A 3D Canopy Radiative Transfer Model for Global Climate Modeling: Description, Validation, and Application

HUA YUAN,* ROBERT E. DICKINSON,+ YONGJIU DAI,# MUHAMMAD J. SHAIKH,+ LIMING ZHOU,@ WEI SHANGGUAN,# AND DUOYING JI#

* School of Geography, Beijing Normal University, Beijing, China, and Department of Geological Sciences, University of Texas at Austin, Austin, Texas
+ Department of Geological Sciences, University of Texas at Austin, Austin, Texas
# College of Global Change and Earth System Science, Beijing Normal University, Beijing, China
@ Department of Atmospheric and Environmental Sciences, University at Albany, State University of New York, Albany, New York

(Manuscript received 5 March 2013, in final form 16 September 2013)

ABSTRACT

The process of solar radiative transfer at the land surface is important to energy, water, and carbon balance, especially for vegetated areas. Currently the most commonly used two-stream model considers the plant functional types (PFTs) within a grid to be independent of each other and their leaves to be horizontally homogeneous. This assumption is unrealistic in most cases. To consider canopy three-dimensional (3D) structural effects, a new framework of 3D canopy radiative transfer model was developed and validated by numerical simulations and shows a good agreement. A comparison with the two-stream model in the offline Community Land Model (CLM4.0) shows that an increase of canopy absorption mainly happens with sparse vegetation or with multilayer canopies with a large sun zenith angle θ_{sun} and is due to increases of the ground and sky shadows and of the optical pathlength because of the shadow overlapping between bushes and canopy layers. A decrease of canopy absorption occurs in densely vegetated areas with small θ_{sun}. For a one-layer canopy, these decreases are due to crown shape effects that enhance the transmission through the canopy edge. For a multilayer canopy, aside from these shape effects, transmission is also increased by the decreased ground shadow due to the shadow overlapping between layers. Ground absorption usually changes with opposite sign as that of the canopy absorption. Somewhat lower albedos are found over most vegetated areas throughout the year. The 3D model also affects the calculation of the fraction of sunlit leaves and their corresponding absorption.

1. Introduction

The absorption of solar radiation on the land surface is important for determining energy, water, and carbon balances. How vegetation contributes to this absorption is an important question. For modeling, three components of this process need to be calculated, that is, reflected, absorbed, and transmitted radiation, as characterized by the parameters albedo, canopy absorption, and ground absorption, respectively. Albedo is most readily observed by the remote sensing community (Schaaf et al. 2002) and has already been used as a constraint for land surface models (Lawrence and Chase 2007). However, the other two components of the incident radiation (i.e., the absorption by the canopy and ground) are also very important and need to be determined. Climate models usually divide the canopy within a grid into different tiles for plant functional types (PFTs) and bare soil. Two approaches have been used for determining each radiation component, that is, either a lookup table that requires good prior knowledge, such as in the Biosphere–Atmosphere Transfer Scheme (BATS) model (Dickinson et al. 1986), or a one-dimensional (1D) physical process model. Three major types of 1D models were summarized by Wang (2003); the most commonly used is the two-stream model (Dickinson 1983; Sellers 1985; Sellers et al. 1996; Bonan 1996; Dai et al. 2004). The 1D models usually assume that each PFT is isolated from any other and is 100% homogeneously distributed within its land fractional coverage f_c in the grid and that the properties of the

Corresponding author address: Hua Yuan, School of Geography, Beijing Normal University, No. 19, Xinjiekouwai Street, Beijing 100875, China.
E-mail: yuanhua@bnu.edu.cn

DOI: 10.1175/JCLI-D-13-00155.1

three radiation components are just the average of those of each PFT weighted by the f_c values.

The homogeneous representation of canopy structure, as noted above, is unrealistic in most cases. For example, in savannas or other sparsely vegetated areas, canopies are usually widely spaced with gaps in between. Another example is the boreal region, where multiple layers (trees, shrubs, and grasses) at different vertical levels may coexist. More direct evidence of the heterogeneity of canopies is seen in the Moderate Resolution Imaging Spectroradiometer (MODIS) Vegetation Continuous Fields (VCF) products (Hansen et al. 2003), which contain proportional estimates for three cover types (trees, herbaceous, and bare ground) at 500 m × 500 m resolution. The statistical results from the VCF dataset show that, over all land, the percentage of grids in which the percent bare soil cover >95% is 21.29%, mostly from the contributions of deserts; the percent herbaceous cover >95% is just 3.40%; and the percent tree cover >95% is only 0.03%. High percentages of tree cover, even after converting to the crown cover [dividing by 0.8 as suggested by Hansen et al. (2003)] are infrequent. That is to say, 100% coverage of any type is rare even at high resolution (500 m) on the land surface. Rather, in most cases PFTs coexist with each other. Even without considering the heterogeneity of a single canopy [i.e., its three-dimensional (3D) effects], the two-stream model cannot readily treat the actual system due to its unrealistic assumptions and may introduce a large bias, even possibly resulting in deficiencies of the climate simulation.

The remote sensing community has recognized the importance of 3D geometry and applied some detailed treatments to retrieve the albedo and leaf area index (LAI) parameters (Li and Strahler 1985; Knyazikhin et al. 1998; Schaaf et al. 2002; Myneni et al. 2002), but these treatments have not been translated into simple analytical solutions suitable for climate models. On the other hand, the concepts of gap probability and clumping index (Nilson 1971; Norman and Welles 1983; Li and Strahler 1988; Chen and Black 1991) have been introduced to take into account the 3D effects of canopy, for example, through the geometric optical–radiative transfer (GORT) model (Li et al. 1995), which has been further developed by combining with a two-stream model, such as the Ecological Assimilation of Land and Climate Observations (EALCO) model (Wang 2005) and the Analytical Clumped Two-Stream (ACTS) model (Ni-Meister et al. 2010), now being used in ecosystem models. Another approach proposed by Pinty et al. (2004a, 2006) is to use effective leaf optical properties and LAI, instead of true values, as fitting parameters incorporated into the two-stream model to match the numerical results. Both approaches are equivalent in modifying the optical properties in a 1D model. However, they require good estimates of clumping indices or effective optical properties under all kinds of conditions.

Climate models run their computations on a global mesh with as high resolution as is feasible. In addition, with the advent of global quantitative derivation of terrestrial properties by remote sensing in terms of types, resolution, and accuracy, a more detailed description of radiative transfer processes on the land surface is both possible and necessary. This paper establishes the construction of a 3D canopy radiative transfer model that takes into account the horizontal and vertical heterogeneities of the canopy, but with a simple physically based formulation that has computational efficiency comparable to that of the 1D model it replaces. This 3D model is a new framework based on the single bush model (Dickinson et al. 2008; Dickinson 2008). A one-layer canopy model is constructed that considers shadows, intercanopy interactions, and the consequences of low sun (elevation) angles. It is used to build a three-layer canopy that considers shadows overlapping between layers. Two types of numerical simulations are carried out to validate the 3D model and its components, that is, the single bush and one-layer and three-layer models. This 3D model is applied and implemented into the Community Land Model (CLM4.0) (Oleson et al. 2010) and compared with the default two-stream model. Major differences are explicitly described and explained from a 3D viewpoint.

All canopy radiation modeling is founded on principles of ray tracing geometric optics, although in simple cases, as in the 1D two-stream model, it can be expressed in terms of differential equations. The modeling here is directly in terms of geometric optical reasoning. Simple 1D canopies are constructed from leaf optical properties and statistical models of leaf distribution. In 3D, one more level of organization is included (i.e., statistical models of bush distribution).

2. Model description

a. Single bush model

The single bush model starting point was developed earlier (Dickinson et al. 2008; Dickinson 2008). Its basic assumptions are that the bush is a spherical object and that the leaves within it are homogeneous and have a spherical leaf angle distribution (LAD). Optical depth (τ) along the radius of single bush is designated τ_0 and derived from LAI of a single bush as $\tau_0 = (3/8)\text{LAI}$. When the stem area index (SAI) is considered, $\tau_0 = (3/8)(\text{LAI} + \text{SAI})$. Individual leaves were initially treated as isotropic scatterers with a single scatter albedo ω. For incident direct radiation from an overhead sun, the

single bush model determines analytically various bush optical properties, that is, the direct transmission $T_{d,s}$, first-order scattering Φ_1, second-order scattering Φ_2, and higher-order scattering Φ_{3+} phase functions. These are all functions of τ, and scattering phase functions depend on the out-scattering angle θ_{out} as well. Further improvements are made in the first-order scattering to consider individual leaves as bi-Lambertian scatterers (with optical properties of reflectance r and transmittance t). Since bi-Lambertian scattering has only minor effects on the second- and higher-order scattering, we continue to assume isotropic leaf scattering for their calculations. We integrate the total scattering phase function Φ over the upward and downward hemispheres, considering the incident direct radiation at a sun zenith angle θ_{sun} ($\mu = \cos\theta_{\text{sun}}$) to get the single bush albedo α_s and diffuse transmission $T_{i,s}$ respectively, as summarized in appendix A.

Numerical simulation shows that the scattering properties of incident diffuse radiation for a single bush are adequately equivalent to that of incident direct radiation with $\theta_{\text{sun}} = 60°$. So this approximation is used to deal with the diffuse case.

b. One-layer canopy model

Our one-layer canopy consists of many individual single bushes, which are placed in a random distribution horizontally without any overlap of vertical projections and has a fractional cover f_c (the percentage of vertically projected area of the canopy crowns). The area of shadows cast by the bushes on the ground (ground shadow) without overlap is $S_0 = f_c/\mu$, which also applies to multiple bushes with overhead sun or for very small f_c. For a low enough sun angle, shadows start to overlap, and the total shadow area with overlap is modified by statistical modeling to

$$S = \frac{1 - e^{-f_c/\mu}}{1 - f_c e^{-1/\mu}}. \tag{1}$$

The overlap of shadows will increase the average optical depth compared to that of a single bush (i.e., the optical depth for the one-layer canopy is correspondingly increased to $\tau = \tau_0 S_0/S$).

A larger θ_{sun} not only leads to more overlap of shadows, but also to changes of the illumination of the incident direct radiation to be more concentrated at the top part of spherical bushes. With an increase of θ_{sun}, the conditions of illumination become more like that of a 1D case and albedo will increase. Dickinson (1983) addressed this issue in discussing the albedo calculation of a semi-infinite canopy. Unfortunately, the single bush model cannot easily capture this feature. We account for the increment of albedo α_L due to the low sun angle effects using a similar approach following the 1D case of Dickinson (1983) approximated as

$$\alpha_L = (N-1)\alpha_s(\mu = 1, \tau_0) f_c \left(\frac{1}{S} - \frac{1}{S_0}\right), \tag{2}$$

where N is the multiplicative factor of albedo at a θ_{sun} compared with albedo in the overhead sun case ($\theta_{\text{sun}} = 0°$ and $\mu = \cos\theta_{\text{sun}} = 1$) for a semi-infinite canopy. It is a function of θ_{sun} and can be up to about 3 in the visible (VIS) domain and 2 in the near-infrared (NIR) domain. The term α_s ($\mu = 1, \tau_0$) is the single bush albedo with $\theta_{\text{sun}} = 0°$ [Eq. (A15), appendix A]. Equation (2) also includes the f_c and shadow overlapping effects. When f_c is very small ($f_c \to 0$), or there are very few overlapped shadows ($S \approx S_0$), then α_L approaches 0 (i.e., the albedo becomes the same as for the single bush case).

With an increase of f_c, the intercanopy interactions become more important and will increase canopy absorption. This additional absorption A_c is estimated simply (cf. appendix B) and decreases the albedo α and T_i. The additional albedo α_L decreases the canopy absorption A and diffuse transmission T_i. After distributing the increased items evenly to the decreased items, the final results of α, T_i, and A for the one-layer canopy are as follows:

$$\alpha = \alpha_s(\mu, \tau) + \alpha_L - 0.5A_c, \tag{3}$$

$$T_i = T_{i,s}(\mu, \tau) - 0.5\alpha_L - 0.5A_c, \tag{4}$$

and

$$A = 1 - \alpha - T_i - T_d, \tag{5}$$

where T_d is direct transmission of the one-layer canopy and calculated as $T_{d,s}(\tau)$ [Eq. (A1), appendix A]. These properties for incident diffuse radiation are calculated for direct $\theta_{\text{sun}} = 60°$. Corresponding values are designated with a star in its superscript, such as α^* and A^*.

The above solutions are constructed for a black ground (100% absorption) and canopy-shaded area only. To determine reflection of the ground (with reflectance r_g), we first calculate the initial radiation reaching it, $T = 1 - S + S(T_d + T_i)$. This term will be reflected by the ground back upward as diffuse radiation. A fraction of this, $r_g T S^* \alpha^*$, is scattered by the canopy back toward the ground, where S^* is the fraction of sky covered by canopy (i.e., sky shadow). Further such ground–canopy reflections can be added in. The radiation reflected between the ground and canopy is a geometric series, and the common ratio q is $r_g S^* \alpha^*$. Hence, the total transmission [T] is $T/(1 - q)$. In the same way, the canopy absorption from multiple reflections

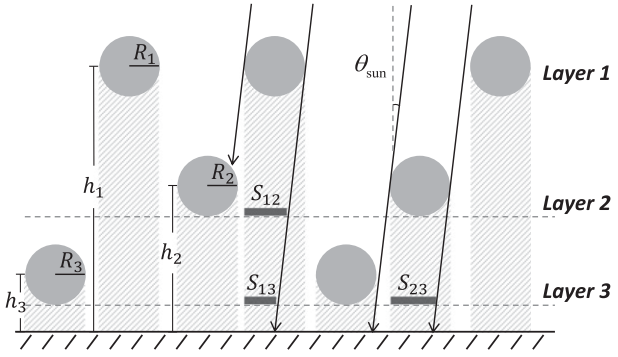

FIG. 1. A sketch of the canopy structures in the 3D canopy model. Bushes of different radii are organized into levels of prescribed heights and randomly spaced at that level. Their interaction is characterized by vertical projections indicated by shaded columns, and shadows indicated by the arrows (i.e., light rays). Self-area shadows on underlying layers are indicated by the *S*'s. Three layers are designed in this study.

between canopy and ground A^m is $r_g TS^*A^*/(1-q)$. The total canopy absorption [A], ground absorption [G], and collective albedo [α] are obtained as

$$[A] = SA + A^m, \tag{6}$$

$$[G] = (1 - r_g)[T], \tag{7}$$

and

$$[\alpha] = 1 - [A] - [G]. \tag{8}$$

A factor *S* before *A* in Eq. (6) is to convert the canopy absorption from the canopy-shaded area to the entire area.

c. Three-layer canopy model

The canopy is divided into three layers. Such division may be based on different PFTs of different heights (e.g., trees, shrubs, and grass) or different age classes (forming upper story, intermediate, and lower story components). Each layer is calculated as a one-layer canopy. In addition, we assume that there is no overlap of vertical projections between the canopy crowns of layers. Each layer has their respective crown radius *R* and central point height *h* as illustrated in Fig. 1. The top canopy layer is designated layer 1, and the bottom layer is designated layer 3. If more than one PFT occurs in a single layer, the layer f_c is the sum of the f_c of the PFTs, and the other canopy properties, such as LAI and ω, are the average of PFTs weighted by their f_c values.

The overlap of shadows between layers is important for the transfer of incident direct radiation, especially in the VIS domain where leaves are highly absorbing. The basic rule followed in treating overlap is that the "self-area shadow" (defined as the shadow area projected on a lower layer overlapped with its vertical projection, such as S_{12}, S_{13}, and S_{23} in Fig. 1) projected on a lower layer cannot overlap with the lower layer's shadow. Otherwise, layer shadows can overlap with each other randomly. The calculation of the self-area shadow is described in appendix C.

We first partition the direct radiation transfer between the different layers and ground. Let $I_{[\text{from}]\to[\text{to}]}$ denote the incident direct radiation (unit source, designated I_0) from layer [from] to layer [to]. The subscript 0 means the position just above the canopy, and *g* means the position just above the ground. The direct radiation from I_0 to each canopy layer or reaching the ground without passing through the canopy is

$$\begin{aligned}
I_{0\to1} &= S_1,\\
I_{0\to2} &= (1 - S_1 + S_{12})S_2,\\
I_{0\to3} &= [1 - (S_1 - S_{13}) - (S_2 - S_{23})\\
&\quad + (S_1 - S_{12})(S_2 - S_{23})]S_3, \quad \text{and}\\
I_{0\to g} &= 1 - S_1 - S_2 - S_3 + (S_1 - S_{12})S_2 + (S_1 - S_{13})S_3\\
&\quad + (S_2 - S_{23})S_3 - (S_1 - S_{12})(S_2 - S_{23})S_3,
\end{aligned} \tag{9}$$

where $S_{[n]}$ represents the shadow of layer *n*. The direct radiation to layer 1 can further transmit directly to lower layers, which are calculated as

$$\begin{aligned}
I_{1\to2} &= T_{d,1}(S_1 - S_{12})S_2,\\
I_{1\to3} &= T_{d,1}[S_1 - S_{13} - (S_1 - S_{12})(S_2 - S_{23})]S_3, \quad \text{and}\\
I_{1\to g} &= T_{d,1}[S_1 - (S_1 - S_{12})S_2 - (S_1 - S_{13})S_3\\
&\quad + (S_1 - S_{12})(S_2 - S_{23})S_3],
\end{aligned} \tag{10}$$

where $T_{d,1}$ is the direct transmission of layer 1. In the same way, we can get

$$\begin{aligned}
I_{2\to3} &= T_{d,2}(I_{0\to2} + I_{1\to2})\frac{(S_2 - S_{23})S_3}{S_2},\\
I_{2\to g} &= T_{d,2}(I_{0\to2} + I_{1\to2})\frac{S_2 - (S_2 - S_{23})S_3}{S_2},
\end{aligned} \tag{11}$$

and

$$I_{3\to g} = T_{d,3}(I_{0\to3} + I_{1\to3} + I_{2\to3}). \tag{12}$$

Adding the above results, the accumulated direct radiation to each layer is

$$
\begin{aligned}
I_1 &= I_{0\to1},\\
I_2 &= I_{0\to2} + I_{1\to2},\\
I_3 &= I_{0\to3} + I_{1\to3} + I_{2\to3}, \quad \text{and}\\
I_g &= I_{0\to g} + I_{1\to g} + I_{2\to g} + I_{3\to g}.
\end{aligned} \tag{13}
$$

The fraction of direct radiation absorbed as direct by layer n is given by the product of radiation attenuated and fraction of attenuated radiation that is directly absorbed:

$$I_n(1 - T_{d,n})(1 - \omega_n). \tag{14}$$

The P_{sun}, fraction of canopy top exposed to sunlight, for layer n is calculated by dividing the accumulated direct radiation by its shadow area:

$$P_{\text{sun}} = I_n / S_n. \tag{15}$$

For the top layer, $P_{\text{sun}} = 1$, which means a 100% sunlit cover. For a lower layer, P_{sun} can be less than 1 if shaded by the upper layers. In this case, it means the available incident direct radiation is modified and the fractions of sunlit LAI (F_{sun}) will be further affected. The quantity P_{sun} was used in a revised F_{sun} (section 4a).

The major calculation process of the three-layer model uses a system of linear equations. Six variables, $I^*_{\uparrow,1}$, $I^*_{\downarrow,1}$, $I^*_{\uparrow,2}$, $I^*_{\downarrow,2}$, $I^*_{\uparrow,3}$, and $I^*_{\downarrow,3}$ as shown in Fig. 2, are chosen as the unknowns. They stand for the total upward and downward diffuse radiation flux of corresponding layers noted by the subscript $[n]$. The value of $I^*_{[\uparrow,\downarrow],[n]}$ is the result of both transmission and reflection of the layer n and can be expressed as follows:

$$I^*_{\uparrow,1} = I_1\alpha_1 + I^*_{\uparrow,2}S^*_1T^*_{i,1} + I^*_{\uparrow,2}(1 - S^*_1) + I^*_0S^*_1\alpha^*_1, \tag{16a}$$

$$I^*_{\downarrow,1} = I_1T_{i,1} + I^*_0S^*_1T^*_{i,1} + I^*_0(1 - S^*_1) + I^*_{\uparrow,2}S^*_1\alpha^*_1, \tag{16b}$$

$$I^*_{\uparrow,2} = I_2\alpha_2 + I^*_{\uparrow,3}S^*_2T^*_{i,2} + I^*_{\uparrow,3}(1 - S^*_2) + I^*_{\downarrow,1}S^*_2\alpha^*_2, \tag{16c}$$

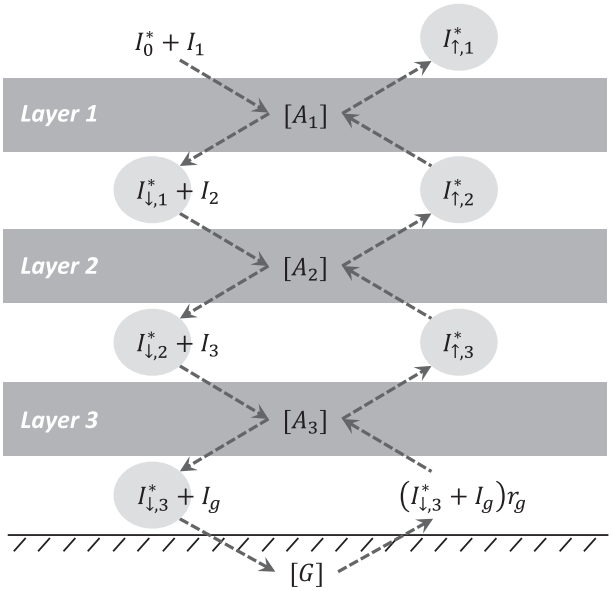

FIG. 2. A sketch of the three-layer canopy model calculation.

$$I^*_{\downarrow,2} = I_2T_{i,2} + I^*_{\downarrow,1}S^*_2T^*_{i,2} + I^*_{\downarrow,1}(1 - S^*_2) + I^*_{\uparrow,3}S^*_2\alpha^*_2, \tag{16d}$$

$$I^*_{\uparrow,3} = I_3\alpha_3 + (I^*_{\downarrow,3} + I_g)r_gS^*_3T^*_{i,3} + (I^*_{\downarrow,3} + I_g)r_g(1 - S^*_3) + I^*_{\downarrow,2}S^*_3\alpha^*_3, \tag{16e}$$

and

$$I^*_{\downarrow,3} = I_3T_{i,3} + I^*_{\downarrow,2}S^*_3T^*_{i,3} + I^*_{\downarrow,2}(1 - S^*_3) + (I^*_{\downarrow,3} + I_g)r_gS^*_3\alpha^*_3, \tag{16f}$$

where I^*_0 stands for the incident diffuse radiation that is also considered as the unit source. For the incident direct radiation case, $I^*_0 = 0$ and $I_{[n]}$ is precalculated [Eq. (13)]. For incident diffuse radiation case, $I^*_0 = 1$ and $I_{[n]} = 0$. Equations (16a)–(16f) represent an equilibrium state, which means the multiple reflections and transmissions between layers have been taken into account. After a simple transformation of Eqs. (16a)–(16f), the matrix forms can be expressed as

$$\begin{pmatrix}
1 & -\tilde{T}_1 & & & & \\
1 & -\tilde{\alpha}_1 & & & & \\
-\tilde{\alpha}_2 & 1 & & -\tilde{T}_2 & & \\
-\tilde{T}_2 & & 1 & -\tilde{\alpha}_2 & & \\
 & & -\tilde{\alpha}_3 & 1 & -\tilde{T}_3r_g & \\
 & & -\tilde{T}_3 & & 1 - r_g\tilde{\alpha}_3
\end{pmatrix}
\begin{pmatrix}
I^*_{\uparrow,1}\\ I^*_{\downarrow,1}\\ I^*_{\uparrow,2}\\ I^*_{\downarrow,2}\\ I^*_{\uparrow,3}\\ I^*_{\downarrow,3}
\end{pmatrix}
=
\begin{pmatrix}
I_1\alpha_1\\ I_1T_{i,1}\\ I_2\alpha_2\\ I_2T_{i,2}\\ I_3\alpha_3 + I_gr_g\tilde{T}_3\\ I_3T_{i,3} + I_gr_g\tilde{\alpha}_3
\end{pmatrix}, \tag{17}$$

for the incident direct radiation case, and

$$\begin{pmatrix} 1 & -\tilde{T}_1 & & & & \\ & 1 & -\tilde{\alpha}_1 & & & \\ -\tilde{\alpha}_2 & 1 & & -\tilde{T}_2 & & \\ -\tilde{T}_2 & & 1 & -\tilde{\alpha}_2 & & \\ & & -\tilde{\alpha}_3 & 1 & -\tilde{T}_3 r_g & \\ & & -\tilde{T}_3 & & 1-r_g\tilde{\alpha}_3 & \end{pmatrix} \begin{pmatrix} I^*_{\uparrow,1} \\ I^*_{\downarrow,1} \\ I^*_{\uparrow,2} \\ I^*_{\downarrow,2} \\ I^*_{\uparrow,3} \\ I^*_{\downarrow,3} \end{pmatrix} = \begin{pmatrix} I^*_0\tilde{\alpha}_1 \\ I^*_0\tilde{T}_1 \\ 0 \\ 0 \\ 0 \\ 0 \end{pmatrix}, \tag{18}$$

for incident diffuse radiation case, where $\tilde{\alpha}_n = S^*_n\alpha^*_n$ and $\tilde{T}_n = S^*_nT^*_n - S^*_n + 1$. The matrices of coefficients in Eqs. (17) and (18) are the same, each with a 6×6 matrix (the 0 elements are shown with blanks). Thus, we can combine the two equations in a simple matrix form:

$$\mathbf{AX} = \mathbf{B}, \tag{19}$$

where $\mathbf{A}$ contains the common coefficients. The matrix $\mathbf{X} = (\mathbf{x}, \mathbf{x}^*)$ consists of two column vectors, that is, the solutions for direct [Eq. (17)] and diffuse [Eq. (18)] radiation. The matrix $\mathbf{B} = (\mathbf{b}, \mathbf{b}^*)$ also consists of two column constant vectors for the direct and diffuse radiation, respectively.

There are many algorithms for solving Eq. (19). We chose Gaussian elimination with slight modifications. There are three beneficial characteristics of Eq. (19). One is that the diagonal elements in the matrix $\mathbf{A}$ are already the pivots, which means it is not necessary to find the largest absolute value of each column and exchange rows to move the entry to the pivot position during the elimination processes. Another one is that there are lots of 0 elements in the $\mathbf{A}$, which means less row reductions are needed. The last one is that the direct and diffuse radiation can be solved for the same operations. Normally, Eq. (19) has a solution under all conditions (e.g., missing layers exist) unless two 1.0 values occur in a row for values $\tilde{\alpha}_1$, $\tilde{\alpha}_2$, $\tilde{\alpha}_3$, and r_g. However, this situation is not expected to happen under natural conditions. After solving for $\mathbf{X}$, the albedo and absorption for each layer and ground can be written as

$$\begin{aligned} [\alpha] &= I^*_{\uparrow,1}, \\ [A_1] &= I_1A_1 + I^*_{\uparrow,2}S^*_1A^*_1, \\ [A_2] &= I_2A_2 + (I^*_{\downarrow,1} + I^*_{\uparrow,3})S^*_2A^*_2, \\ [A_3] &= I_3A_3 + [I^*_{\downarrow,2} + (I_g + I^*_{\downarrow,3})r_g]S^*_3A^*_3, \quad \text{and} \\ [G] &= (I_g + I^*_{\downarrow,3})(1 - r_g), \end{aligned} \tag{20}$$

for the direct case, and

$$\begin{aligned} [\alpha^*] &= I^*_{\uparrow,1}, \\ [A^*_1] &= S^*_1A^*_1 + I^*_{\uparrow,2}S^*_1A^*_1, \\ [A^*_2] &= (I^*_{\downarrow,1} + I^*_{\uparrow,3})S^*_2A^*_2, \\ [A^*_3] &= [I^*_{\downarrow,2} + (I_g + I^*_{\downarrow,3})r_g]S^*_3A^*_3, \quad \text{and} \\ [G^*] &= I^*_{\downarrow,3}(1 - r_g), \end{aligned} \tag{21}$$

for the diffuse case. All the PFTs, including bare soil, share the same albedo and ground absorption. Each PFT within a layer shares the same P_{sun} as calculated in Eq. (15). The layer absorption, as well as the direct radiation absorbed as direct, is distributed to its PFTs according to the weights calculated by the individual PFT results using the one-layer model.

3. Numerical validation

Two types of numerical simulations were performed to validate the 3D canopy model against more detailed computation. One is the full (optical) path (FP) simulation, and the other is the Monte Carlo (MC) simulation. For the FP simulation, we divided the spherical bush into small unit cubes (30 cubes along the radius) with equal sizes in Cartesian coordinates. Each cube performs as an individual volume of leaves that can both absorb and scatter radiation as a point source. The FP can simulate each order of scattering of a single bush effectively because it can more easily achieve a steady state than the MC simulation, especially for higher-order scattering. The MC simulation follows North (1996)'s formulation, but with more details for 3D canopy structures and the radiation recording. It was implemented in a 100 m $\times$ 100 m square size area, and 100 million uniformly spaced photons were generated as direct or diffuse radiation incident on the top of the canopy. Compared with the FP simulation, the MC is more effective at the simulation of a 3D canopy with complicated structures. It was also used to simulate a single bush for mutual validation of the FP and MC simulations (i.e., to make sure of the correctness of both simulations). Neither simulation accounts for the hot-spot effect, which makes but a minor contribution to

TABLE 1. Comparison between MC and FLIGHT for a RAMI1–3 baseline scenario. The results are averages of 100 simulations and the numbers in parentheses are the standard deviations.

	θ_{sun}	Band	MC	FLIGHT	Difference
Albedo	20°	Red	0.0410 (0.0001)	0.0412 (0.0001)	−0.0002
		NIR	0.2853 (0.0004)	0.2849 (0.0005)	0.0004
	50°	Red	0.0337 (0.0001)	0.0338 (0.0001)	−0.0001
		NIR	0.3401 (0.0004)	0.3396 (0.0004)	0.0005
Canopy absorption	20°	Red	0.4650 (0.0002)	0.4647 (0.0010)	0.0003
		NIR	0.1033 (0.0002)	0.1027 (0.0008)	0.0006
	50°	Red	0.6022 (0.0003)	0.6023 (0.0010)	−0.0001
		NIR	0.1336 (0.0003)	0.1330 (0.0009)	0.0006
Ground absorption	20°	Red	0.4940 (0.0002)	0.4941 (0.0009)	−0.0001
		NIR	0.6113 (0.0004)	0.6116 (0.0011)	−0.0003
	50°	Red	0.3642 (0.0003)	0.3639 (0.0009)	0.0002
		NIR	0.5263 (0.0004)	0.5265 (0.0013)	−0.0002

the albedo calculation but affects some remote sensing issues.

To benchmark the MC simulation, we compared it with a Forest Light interaction model (FLIGHT), version 5.0 (North 1996), in a baseline scenario in the canopy Radiation Transfer Model Intercomparison (RAMI) exercise phases 1, 2, and 3 (Pinty et al. 2001, 2004b; Widlowski et al. 2007). This scene contains 15 floating canopy spheres treated as a turbid medium. For details of the parameter setting, refer to Pinty et al. (2001; or the website http://rami-benchmark.jrc.ec.europa.eu). Four experiments were simulated with two θ_{sun} (20° and 50°) in two bands. We ran MC and FLIGHT both 100 times for each experiment. The results are shown in Table 1. The absolute values of the mean differences in albedo, canopy absorption, and ground absorption are all less than 0.001. The MC and FP were compared in simulating the first- and second-order scattering phase functions of a single spherical bush. Figure 3 gives an example of the scattering phase function of two angles. The mean differences for different LAI values between the MC and FP are an order of 0.001 or less.

a. Single bush model validation

The FP simulation was used to validate the single bush model, for the very simple case in which the leaves within the spherical bush are isotropic scatterers and the sun is overhead. The normalized first-order, second-order, and higher-order scattering phase functions (Φ_1, Φ_2, and Φ_{3+}, respectively) from the 3D model, FP, and their differences are shown in Fig. 4. Only Φ_{3+} depends on ω. The figure shows that the differences of Φ_1 and Φ_2 compared with FP are all within 0.05, while Φ_{3+} has a larger bias (>0.10) in the large LAI (>6) case, resulting from the assumption of isotropic scattering of Φ_{3+}. Since all these results are normalized, by being multiplied by a factor ($0.25\omega/\pi$ for Φ_1 and $0.25\omega^2/\pi$ for Φ_2 and Φ_{3+}), the actual biases are much smaller, especially for the VIS domain in which ω is small. More accurate formulations are possible for the single bush model, but in fact its bias is already much less than that originating from the canopy horizontal and vertical structures. Therefore, we maintain simplicity, allowing analytic integrals for the albedo and diffuse transmission.

b. One-layer canopy model validation

The one-layer canopy model was tested for seven f_c values (0.1, 0.2, . . . , 0.7), ten values of θ_{sun} (0°, 10°, . . . , 80° and diffuse radiation) and three LAI (1, 3, and 6) values. Leaves are bi-Lambertian scatterers and have a spherical LAD. The average radius $\overline{R}$ and height $\overline{h}$ of bushes were preset. The radius R and height h values are assumed to have normal distributions of $R \sim N(\overline{R}, \sigma = 0.2\overline{R})$ and $h \sim N(\overline{h}, \sigma = 0.2\overline{h})$. For each case, we generate 100 samples from MC simulations and use

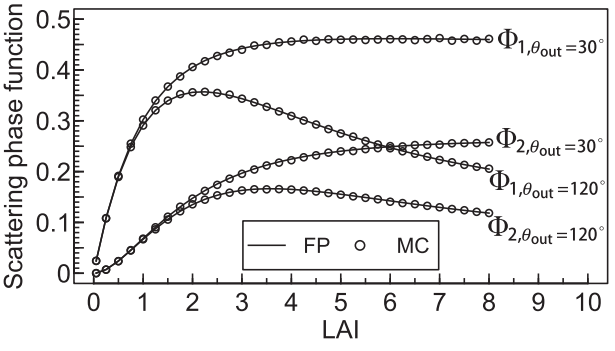

FIG. 3. Comparison of first-order (Φ_1, normalized by dividing by $0.25\omega/\pi$) and second-order scattering phase function (Φ_2, normalized by dividing by $0.25\omega^2/\pi$) at out-scattering angles 30° and 120° (θ_{out}, defined relative to the vertical direction, going from 0 for backward direction to π for forward direction) between FP and MC simulations for a single spherical bush. Leaves are isotropic scatterers with $\omega = 0.85$.

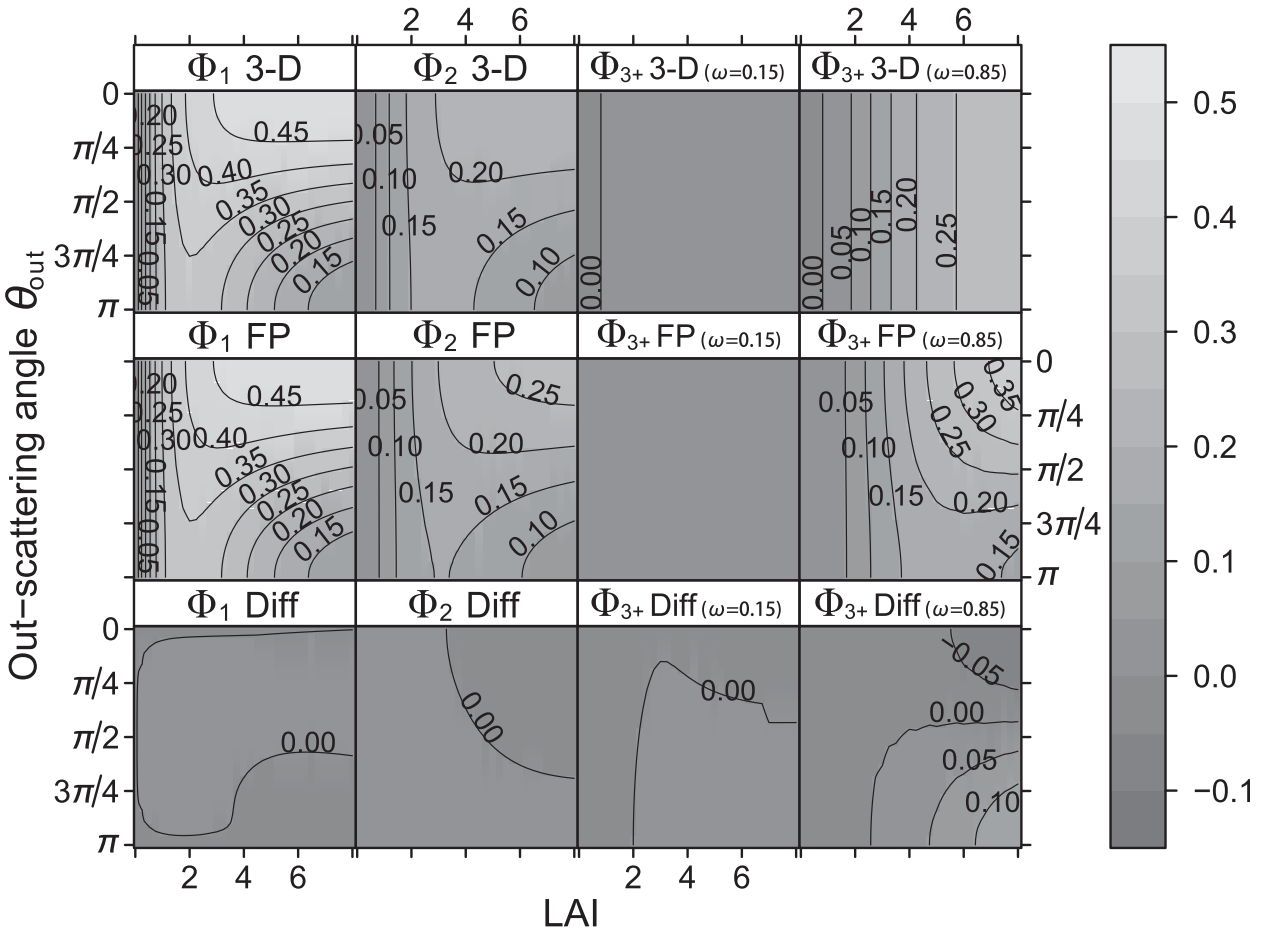

FIG. 4. Normalized scattering phase function for a single bush for the first-order Φ_1, second-order Φ_2, and third- and higher-order scattering Φ_{3+} ($\omega = 0.15$ and 0.85, respectively). The contour plots are their values vs LAI and out-scattering angle θ_{out}. Diff in the bottom panel is 3D model minus FP.

the average results to compare with the 3D model in solid circles of a scatterplot as shown in Fig. 5. The two-stream results are also included as hollow circles.

As seen in Fig. 5, the 3D model agrees well with the results of the MC simulation in terms of albedo [α], canopy absorption [A], and ground absorption [G] for different LAI values and in both spectral domains, especially for the albedo, for which the RMSE are almost always within 0.01 except for the NIR domain at large LAI values. For canopy and ground absorption, the RMSE values are all within 0.04. The RMSE increases with increasing LAI in both spectral domains and overall RMSE of canopy absorption and ground absorption in the VIS domain are both 0.024, and in the NIR domain are 0.020 and 0.026. The corresponding RMSE values of the two-stream model increase to 0.122 and 0.095 in the VIS domain and to 0.068 and 0.059 in the NIR domain. In sum, for the assumed one-layer geometry, the 3D model errors are typically in the range of 0.01–0.02, in some instances a little higher; whereas, the 1D model errors are in the order of 0.1. In some limiting cases both models have small similar errors, that is, the two-stream model behaves similarly to the 3D and MC for small LAI values (LAI = 1) in [α], [A], and [G], as well as in the medium θ_{sun} [$\sim$(30°–60°)] case. For small f_c, the agreement is only apparent, a result of small canopy absorption and albedo.

The 3D model reproduces two features of canopy and ground absorption not given by the two-stream model. One of these is most pronounced at low sun angle (large θ_{sun}) with medium f_c value, and the other is most pronounced at small θ_{sun} with large f_c and LAI values. The first difference is the effects of shadows. Shadowing reduces the radiation reaching the ground, and the sky shadow further reduces the reflected radiation back to the sky. The latter is especially significant for snow cover. The other major difference is the heterogeneity of radiative path lengths. In particular, the radiation can

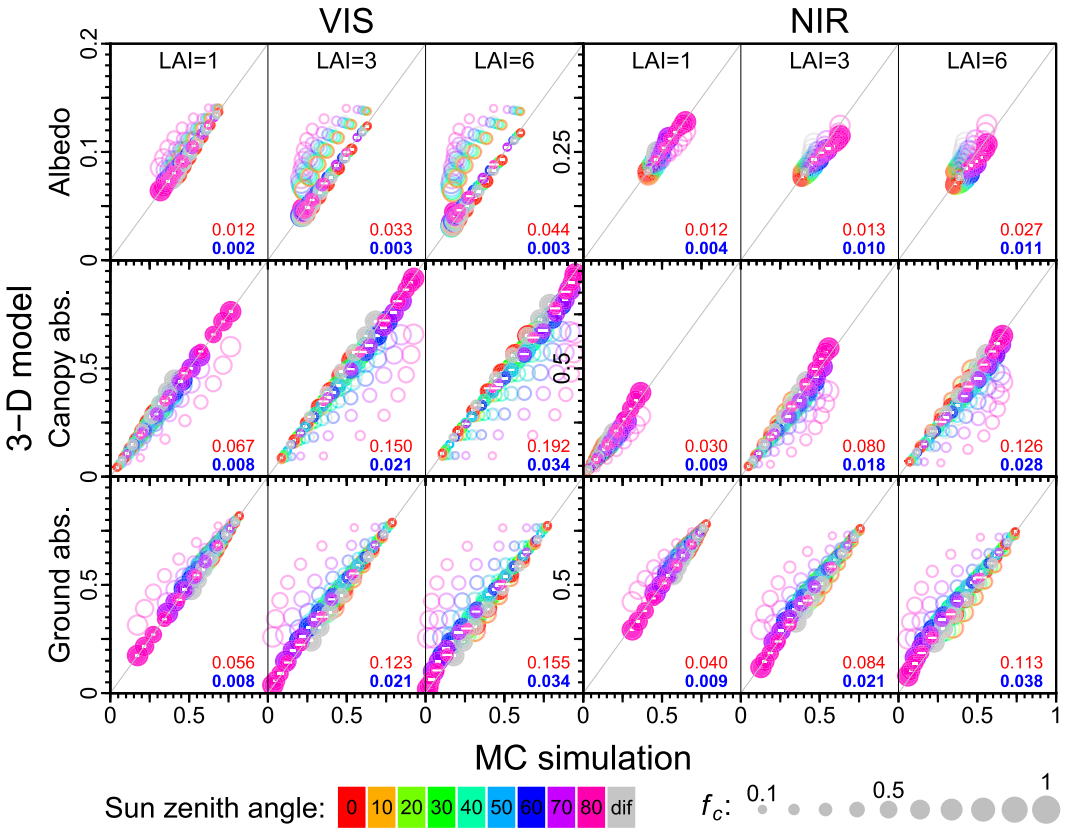

FIG. 5. Scatterplot of one-layer canopy. For the VIS domain, the leaf reflectance r is 0.10, leaf transmittance t is 0.05, and ground reflectance r_g is 0.15; for the NIR domain, r is 0.45, t is 0.25, and r_g is 0.20. The solid circles represent the 3D model results, and hollow circles represent two-stream model results. The circle size represents the f_c value and circle color represents the sun zenith angle as shown in the legend. A white bar in the solid circle stands for the uncertainty of MC simulation. The red number in each plot is the RMSE of the two-stream model compared with MC and the blue one represents the RMSE of the 3D model.

directly pass through or scatter downward from the canopy edge more easily than through its center with less canopy absorption and higher ground absorption, a result of canopy clumping (i.e., canopy shape effects). For the albedo, the two-stream model gets slightly higher values with the increasing LAI values, especially for low sun angle and medium f_c values, and the total RMSE is somewhat larger than that of the 3D model, by 0.029 for VIS and 0.01 for NIR. The differences in the VIS domain are mainly due to the shadow effects since the albedo from the ground contributes far more than the canopy due to the lower reflections of leaves. For albedo in the NIR domain, the situation is a little more complicated because the ground reflectance can be either greater or less than the canopy reflectance. At the same time, the intercanopy interactions and increased transmission due to shape effects can reduce the albedo in the 3D case. Therefore, the final difference between the two-stream model and the 3D model is dependent on the balance of the above effects. In this test, the ground reflectance r_g is set to 0.2, which is similar to the canopy reflectance and the two-stream model shows an overestimated albedo for large LAI.

c. *Three-layer canopy model validation*

We also used MC simulation to validate the three-layer canopy model. The 16 PFTs that are currently being used in CLM4.0 were chosen as inputs (Table 2). The eight types of trees in CLM are allocated to the top layer; the three types of shrubs are allocated to the midlayer; and the remaining five types of grasses and crops are assigned to the bottom layer. The leaf and stem optical properties are the same as in the CLM4.0.

Two types of experiments were used to validate the three-layer canopy model. First, the canopy structures, including f_c, LAI, SAI, $\overline{R}$, and $\overline{h}$ for each PFT, were preset as listed in Table 2. There were three groups of test data in terms of total canopy f_c: 20%, 50%, and 80%. The generation of a canopy scene started from the top layer to the bottom layer, and each layer followed the one-layer case. We tested different θ_{sun} and soil types.

TABLE 2. Prescribed input data for three-layer canopy validation.

Plant functional type		f_c		LAI ($m^2 m^{-2}$)	SAI ($m^2 m^{-2}$)	$\overline{R}$ (m)	$\overline{h}$ (m)
Needleleaf evergreen tree temperate (NETM)	—	0.10	—	2.5	0.4	6	12
Needleleaf evergreen tree boreal (NETH)	—	—	—	2.8	0.5	6	12
Needleleaf deciduous tree boreal (NDTH)	—	0.05	—	4.3	0.9	6	12
Broadleaf evergreen tree tropical (BETL)	—	—	0.30	6.0	0.7	6	12
Broadleaf evergreen tree temperate (BETM)	—	0.05	—	5.4	0.1	6	12
Broadleaf deciduous tree tropical (BDTL)	—	—	0.06	1.1	0.2	6	12
Broadleaf deciduous tree temperate (BDTM)	0.05	—	—	4.3	0.8	6	12
Broadleaf deciduous tree boreal (BDTH)	—	0.15	—	1.9	0.3	6	12
Broadleaf evergreen shrub temperate (BESM)	—	0.05	0.20	2.1	0.6	2	4
Broadleaf deciduous shrub temperate (BDSM)	0.03	—	0.10	2.0	0.5	2	4
Broadleaf deciduous shrub boreal (BDSH)	—	—	—	2.1	0.5	2	4
C_3 Arctic grass (C3A)	0.06	—	—	1.1	0.5	1	1.1
C_3 grass (C3)	—	0.10	—	2.2	0.5	1	1.1
C_4 grass (C4)	—	—	0.14	4.0	0.2	1	1.1
Crop1	0.06	—	—	3.5	0.2	1	1.1
Crop2	—	—	—	—	—	1	1.1

For each case, we also ran 100 samples to identify the uncertainty of the MC simulations. The 3D model results, as well as the two-stream results, are compared in Fig. 6. Evidently, the 3D model reproduces quite well the dependences on θ_{sun} of albedo, PFT absorption, and ground absorption in all three groups, even with NIR and ground snow cover (shown as NIR + Snow in Fig. 6). The differences between the two-stream and 3D model in the one-layer comparisons are also seen in Fig. 6. In addition, there are two other differences: (i) the lower-layer canopy absorbs less radiation with an increase of θ_{sun} due to the upper layer's shadow projection on the lower layer, especially for larger f_c values of upper layers. The two-stream model does not show this feature because it considers all of the PFTs to be isolated without mutual interactions. It also has relative small variations in the absorption of PFTs with θ_{sun}. (ii) The ground absorption can increase slightly with θ_{sun} near 0° for the large f_c as shown in Fig. 6c due to the shadow overlapping between layers that reduces the total ground shadow cover and increases the direct transmission to the ground. Consequently, the ground absorption increases, as is more obvious in the high canopy f_c case. The two-stream shows a monotonic decrease of ground absorption with increase of θ_{sun}.

For the second experiment, we randomly chose several PFTs (≤5 types) and randomly set their f_c (total canopy $f_c \leq 75\%$) and LAI values (≤7). The SAI, $\overline{R}$, and $\overline{h}$ were kept the same as for the first experiment, as shown in Table 2. The scatterplot of 3D model results, as well as two-stream model results, versus MC simulations in different θ_{sun} and background cover types are shown in Fig. 7. As seen in the figure, the 3D model performs much better as indicated by the RMSE values, especially in the NIR + Snow case. The overall RMSE of albedo decreases from the 0.163 of the two-stream model to 0.019, and in the VIS + Soil case, the overall RMSE of ground absorption decreases from the 0.170 of the two-stream model to 0.017. The two-stream model performs relatively better for the small θ_{sun} (e.g., at 0° and 30°) than for large θ_{sun}.

4. Application and comparison

a. Implementation in CLM4.0

Given the classification of vegetated land units in CLM4.0, the 3D model processes all the PFTs within a soil column at a time, including the bare soil type. The PFTs are divided into three layers as described in section 3c. Figure 8 shows statistical results for each layer's percentage, all layers' percentage, and the number of layers existing in each grid as derived from the CLM4.0 input dataset (Lawrence and Chase 2007). The R and h of each PFT are simply calculated from the parameters of canopy top and bottom heights (Z_{top} and Z_{bot}) as prescribed in CLM4.0 (i.e., $R = Z_{top} - Z_{bot}$ and $h = Z_{bot} + R$). The 3D model is then applied for three layers (section 2c) to process all the soil columns. All PFTs within a soil column share the same albedo, and the same transmission (i.e., the same ground absorption). Consequently, the 3D model does not conserve energy at the PFT level, as the two-stream model does, but only at the column level.

In addition, P_{sun} was calculated for each PFT and used to revise the F_{sun} values as $F_{sun} \times P_{sun}$. This modification will affect the sunlit and shaded LAI fractions. Another issue is the fraction of absorbed diffuse radiation in the calculation of sunlit/shaded leaves. Bonan et al. (2011) have pointed out the problem of CLM4.0 that apportions

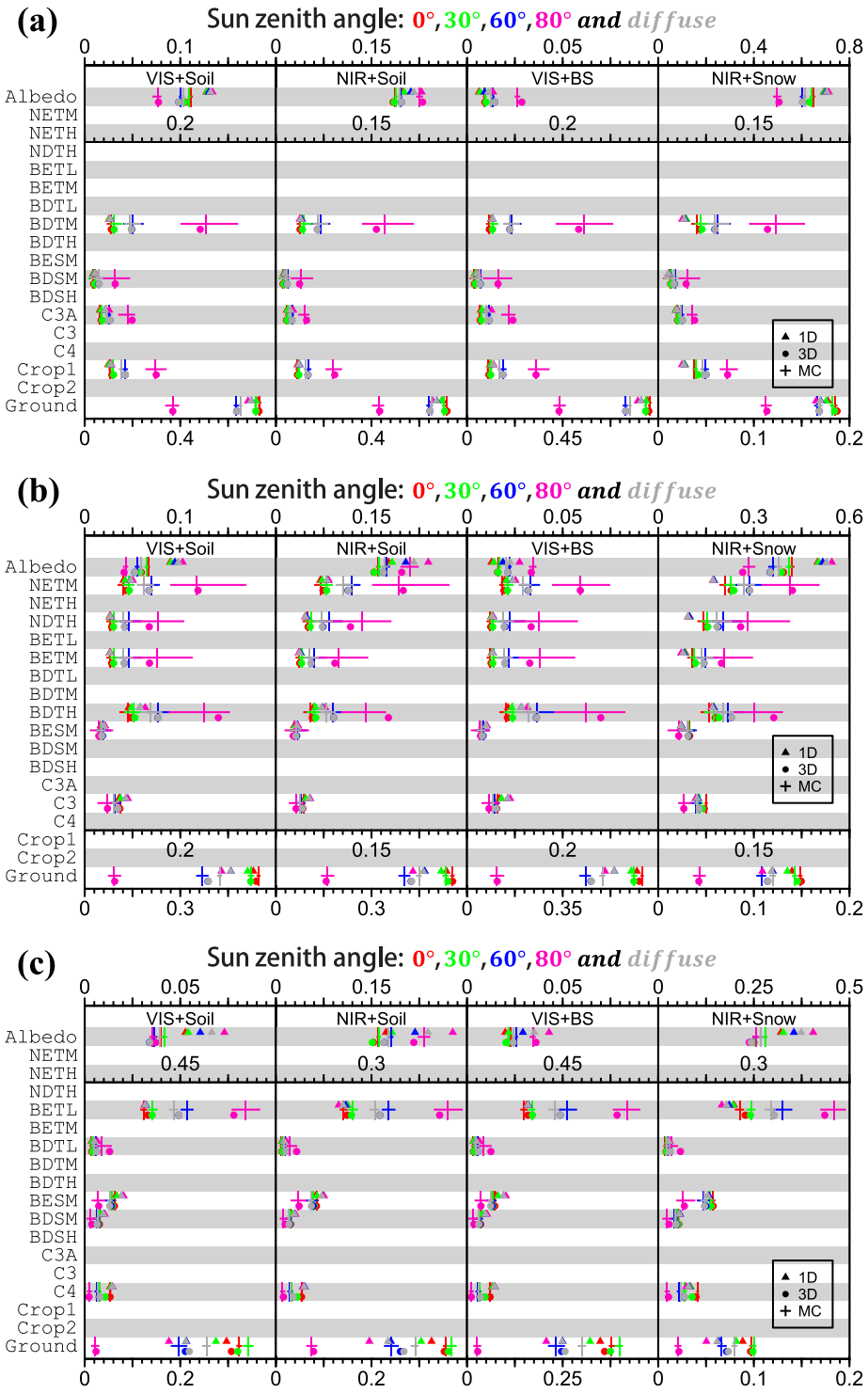

FIG. 6. The X–Y plot of the three-layer canopy results. The total canopy f_c is (a) 20%, (b) 50%, and (c) 80% (details in Table 2). The first line of each plot is the total albedo (for all PFTs and ground, scales refer to the top axis), the following 16 lines represent the absorption of PFTs listed in Table 2 (scales refer to the second axis from the top), and the last line is the ground absorption (scales refer to the bottom axis). The term 1D represents the two-stream model whose results are triangles in the plots, the + symbol represents the MC simulation, the | symbol represents the mean result of 100 samples run, and the − symbol represents the uncertainty. Soil means the background is normal soil cover with $r_g = 0.15$ in VIS domain and $r_g = 0.20$ in the NIR domain; BS stands for black soil (absorption is 100%); and Snow is ground snow cover with $r_g = 0.80$ in the NIR domain.

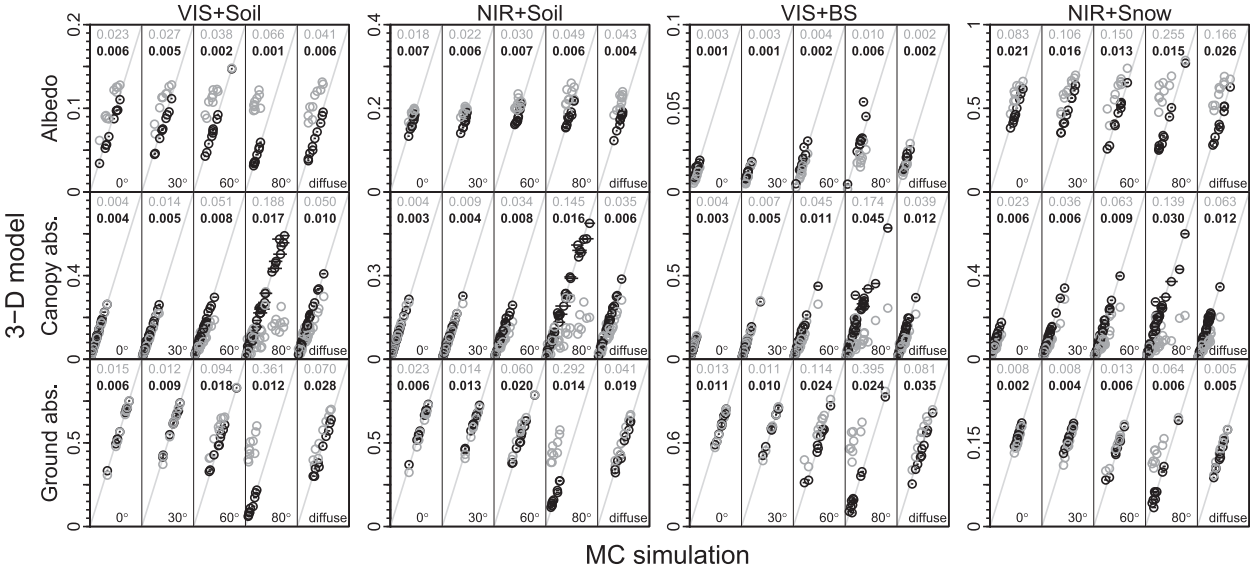

FIG. 7. Scatterplot of the three-layer model results. The dark circles represent the results between the 3D model and MC simulation (uncertainty is plotted as a bar within), and the RMSE is shown with a dark number in the top of each plot. The gray circles represent the two-stream model, and its RMSE number is in gray. The sun zenith angles are labeled at the bottom of each plot. Soil, BS, and Snow are described as in Fig. 6.

the total canopy-absorbed diffuse radiation to sunlit and shaded leaves based on the sunlit (F_{sun}) and shaded fractions ($1 - F_{sun}$) of canopy. In CLM4.0, it assumes that the absorbed diffuse radiation within the canopy is uniformly distributed with a density function of 1/LAI. Here, we modified it to an exponential function as shown in Table 3, and the fraction of absorbed diffuse radiation in sunlit leaves is the result of an integral expression also listed in Table 3. This revision will affect the distribution of absorbed diffuse radiation between sunlit and shaded leaves.

b. Comparison with two-stream model in CLM4.0

We ran the offline CLM4.0 [the National Center for Atmospheric Research (NCAR)'s Community Earth System Model, version 1.0.3 (CESM 1.0.3), with component set "I_2000" with only the land model active and Qian data (Qian et al. 2006) as forcing for current climate conditions at a resolution of $0.9° \times 1.25°$] with the default two-stream model (control run) and 3D canopy radiation model (3D run). Both models ran from 2000 to 2003, and the results of last 3 yr, after 1 yr of spinup, are analyzed below.

1) MONTHLY-MEAN SURFACE SHORTWAVE RADIATION FLUX COMPARISON

The 3D model affects the surface solar radiation flux (shortwave) directly. We compared three components of fluxes, surface-reflected radiation flux F_{sr}, canopy-absorbed radiation flux F_{ca}, and ground-absorbed radiation flux F_{ga}, using the averages of 3-yr monthly-mean results. Their differences in January and July are shown in Fig. 9.

Overall, the F_{sr} of the 3D run, in both January and July, is less than that of control run over most vegetated regions. The differences are about $-2.24\,W\,m^{-2}$ in January and $-3.24\,W\,m^{-2}$ in July averaged over global land. For January, the boreal region with latitudes 50°–60°N shows an increase of F_{ca} and a decrease of F_{sr} compared with the control run. The corresponding difference of F_{ga} is small. In the areas near the equator, such as the Amazon, Congo basin, and Indonesia, the 3D run gets less F_{ca} and F_{sr} and correspondingly gains more F_{ga} ($\sim 10\,W\,m^{-2}$). In relatively sparsely vegetated regions like Sahel, central Australia, the central-western United States, and southern Africa, there are slight increases of F_{ca} and decreases of F_{ga}. For July, the F_{sr} is similar to that for January, but the area with a decrease expands in the Northern Hemisphere. In the boreal region (50°–70°N), the F_{ca}, opposite to the January case, is reduced by about $10\,W\,m^{-2}$ in many places, and the corresponding F_{ga} is higher. The differences in areas near the equator are very similar to that for January. The same as that for January, there are increases of F_{ca} in the areas with relatively sparse vegetation and corresponding decreases in F_{ga} especially obvious in central Asia and the central-western United States. The mean differences over the global land surface of F_{ca} are $-0.04\,W\,m^{-2}$ in January, $-2.36\,W\,m^{-2}$ in July, and the mean differences of F_{ga} are $2.28\,W\,m^{-2}$ for January and $5.61\,W\,m^{-2}$ for July. The statistical results of the

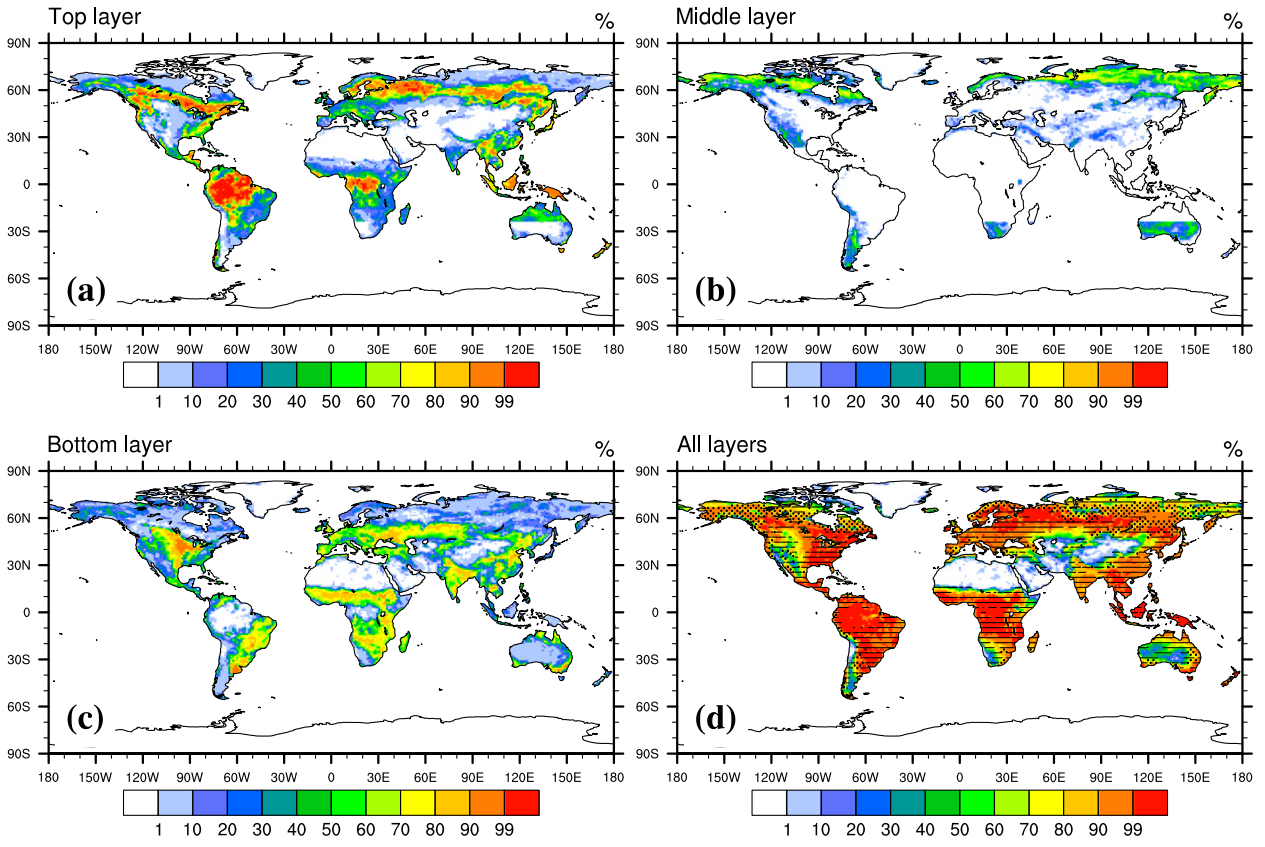

FIG. 8. The statistics of layer percentage at a resolution 0.9° × 1.25°: (a) top, (b) middle, (c) bottom, and (d) all layers. Also shown in (d) are the number of layers in each grid, where a dotted area means three layers covered, lined area means two layers, and no-shaded area means either one layer or no canopy covered. The layer count criterion is the percentage of layer ≥5%.

global-mean values for each month are shown in Table 4. The F_{sr} shows lower values throughout the year. The F_{ca} increases by up to 1.55 W m^{-2} in the early spring, mainly from the contributions of the boreal forest. In the other seasons, F_{ca} shows slightly lower values. The F_{ga} increases throughout the year, especially in summer.

2) DIURNAL CYCLE OF SURFACE RADIATION FLUX COMPARISON

The above comparison is based on time-averaged values and does not provide any details over the diurnal cycle. To better understand how the surface radiation fluxes are changed over the diurnal cycle, we chose three representative regions: the Amazon (0°–10°S, 50°–70°W), the boreal region (50°–70°N), and central Asia (30°–50°N, 50°–80°E). For each grid within the representative region, each model step of a half-hour in local time is averaged for the entire month (January 2003 and July 2003), and the area-averaged values are compared in Fig. 10.

The Amazon is mainly covered by a one-layer canopy (broadleaf tropical trees) and has a high canopy coverage ($f_c \geq 99\%$) (Fig. 8d). The sun orientation changes little over the annual cycle. At local noontime (LN), θ_{sun} is small in both January (the average is 16.1° and the minimum could be 11.0°) and July (the average is 26.6° and the minimum could be 21.7°). With these conditions, the 3D geometry is more able to transmit the radiation

TABLE 3. The fraction of absorbed diffuse radiation in sunlit leaves. The x is the cumulative LAI measured downward from the top of the canopy, and k_b is the direct radiation extinction coefficient of the canopy.

Absorption of diffuse radiation	CLM4.0	Modified*
Density function	$\dfrac{1}{\mathrm{LAI}}$	$\dfrac{e^{-k_b' x}}{\int_0^{\mathrm{LAI}} e^{-k_b' x}\,dx}$
Fraction in sunlit leaves	$\dfrac{\int_0^{\mathrm{LAI}} e^{-k_b x}\,dx}{\mathrm{LAI}}$ (i.e., F_{sun})	$\dfrac{\int_0^{\mathrm{LAI}} e^{-k_b x} e^{-k_b' x}\,dx}{\int_0^{\mathrm{LAI}} e^{-k_b' x}\,dx} P_{\mathrm{sun}}$

*For incident direct radiation, $k_b' = 0.5/\mu$; for incident diffuse radiation, $k_b' = 1$.

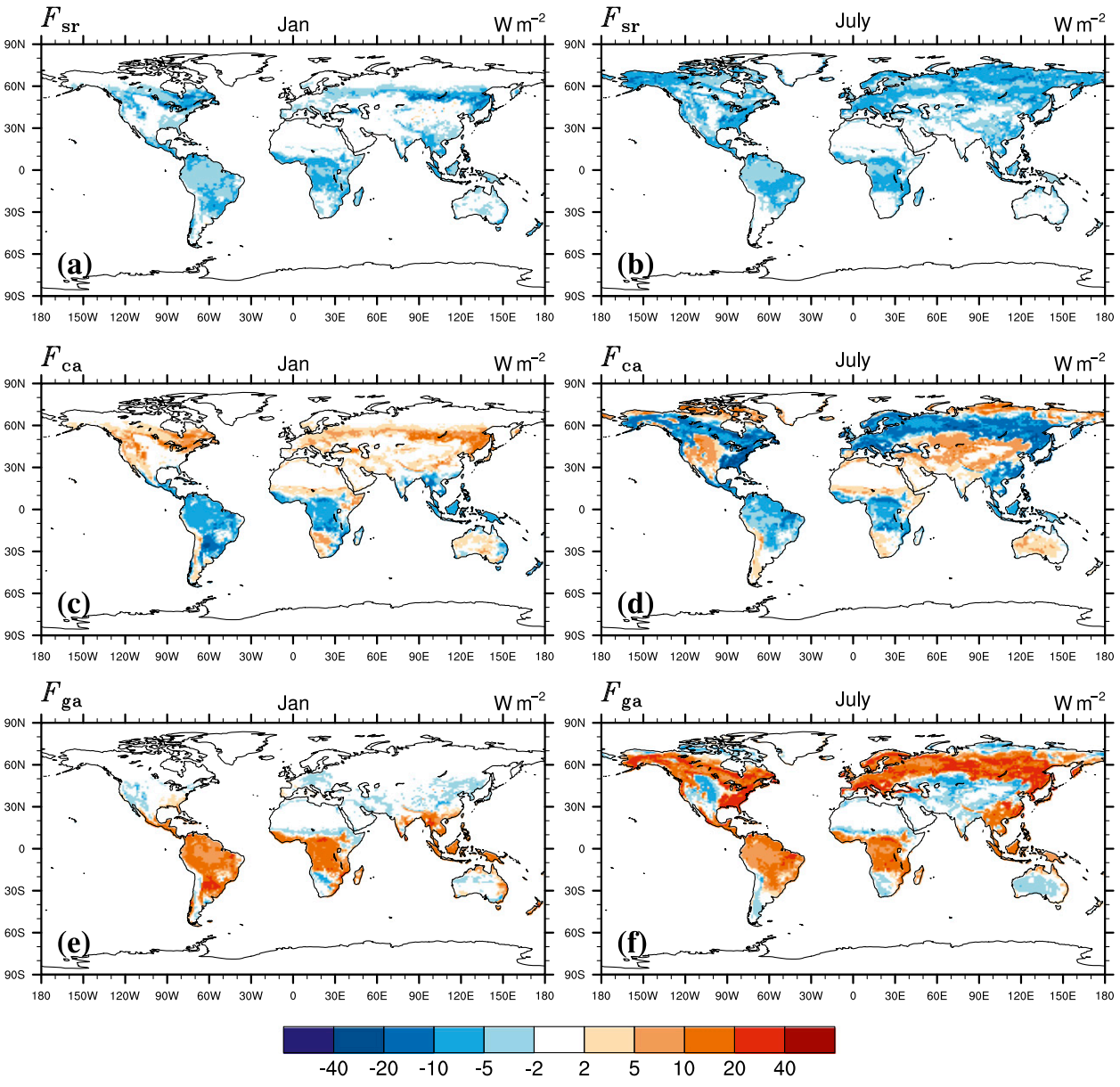

FIG. 9. The difference of surface solar radiation flux (3D run minus control run). (a),(b) F_{sr} is the surface-reflected radiation flux; (c),(d) F_{ca} is the canopy-absorbed radiation flux; and (e),(f) F_{ga} is the ground-absorbed radiation flux: (left) January and (right) July.

through the canopy to the ground, so F_{ga} increases by about 10 W m^{-2} on a daily average (>30 W m^{-2} at LN). The direct transmission of incident direct radiation [T_d] and diffuse transmission of incident diffuse radiation [T_i^*] increase (from heterogeneous paths) as shown in Fig. 10a. Consequently, the F_{ca} and F_{sr} decrease. The decrease of F_{ca} is mainly due to the decrease of the absorption of direct radiation [A], which could be as low as -0.06 in the NIR domain at LN, while the absorption of diffuse radiation [A^*] is similar between the two models. The decrease of F_{sr} is mainly in the NIR domain, and the reduced albedo of incident diffuse radiation [α^*] is more obvious than that of the albedo of incident direct radiation [α]. One feature of the [α] is that the increase of albedo of the 3D model from local noontime to sunset/sunrise is slower (the line is flatter) than that of the two-stream model.

In the boreal region, the canopy cover is dominated by multiple layers (two or three layers; Fig. 8d) and $f_c \geq 90\%$ in most places. In January, the θ_{sun} stays large all day long, increasing the shadow overlapping between layers, as well as the total ground shadow, hence

TABLE 4. Seasonal differences (3D run minus control run) of surface radiation fluxes ($W m^{-2}$) averaged for three regions and global land surfaces.

	Amazon			Boreal			Central Asia			Global land		
Month	F_{sr}	F_{ca}	F_{ga}	F_{sr}	F_{ca}	F_{ga}	F_{sr}	F_{ca}	F_{ga}	F_{sr}	F_{ca}	F_{ga}
January	−3.77	−6.03	9.80	−2.48	2.94	−0.46	−0.58	1.51	−0.93	−2.24	−0.04	2.28
February	−3.59	−6.19	9.78	−6.01	6.89	−0.88	−0.92	1.92	−1.00	−2.99	0.92	2.07
March	−3.63	−6.39	10.01	−9.55	10.72	−1.17	−1.16	2.58	−1.42	−3.68	1.55	2.12
April	−3.96	−6.20	10.15	−8.97	9.31	−0.35	−1.33	3.80	−2.47	−3.60	0.83	2.76
May	−4.17	−5.58	9.75	−5.49	−0.07	5.56	−1.90	4.86	−2.96	−3.13	−1.15	4.28
June	−4.29	−4.97	9.26	−4.91	−6.88	11.78	−2.39	5.47	−3.08	−3.16	−2.42	5.57
July	−4.69	−5.36	10.05	−5.39	−6.80	12.20	−2.29	5.21	−2.92	−3.24	−2.36	5.61
August	−4.86	−6.02	10.88	−4.23	−4.28	8.51	−1.95	4.52	−2.56	−2.89	−1.84	4.72
September	−4.52	−6.96	11.48	−2.72	−1.21	3.93	−1.51	3.69	−2.18	−2.42	−1.24	3.66
October	−4.30	−7.13	11.43	−2.16	1.16	1.00	−0.95	2.71	−1.76	−2.18	−0.78	2.96
November	−4.17	−6.55	10.72	−1.89	2.13	−0.24	−0.56	1.77	−1.21	−2.03	−0.55	2.59
December	−4.07	−6.21	10.28	−1.44	1.71	−0.27	−0.46	1.44	−0.98	−1.96	−0.48	2.43

increasing the canopy absorption and decreasing the transmission to the ground. The reflected radiation from the ground is similarly affected, with a decrease of the F_{sr} in winter and spring because the ground is usually snow covered. The F_{ga} remains unchanged due to lower absorption by snow-covered ground. The maximum difference in F_{ca} is about $12 W m^{-2}$ near the LN. In July, daytime is longer, and the θ_{sun} is about 39.7° on average at LN. For the incident direct radiation, because of the shadow overlapping between layers, the total ground shadow at this time could be less than the total f_c that will increase the $[T_d]$ and decrease the $[A]$ correspondingly. At LN, the increase of F_{ga} is $\sim 35 W m^{-2}$, and the decrease of F_{ca} is $\sim 25 W m^{-2}$. However, at low sun, the situation reverses for the same reason as in January. The time variation of $[A]$ is more like a V shape in the 3D run. For the diffuse case, the differences in $[A^*]$ and $[T_i^*]$ are smaller. The albedo is consistently lower than in the control, especially in the NIR domain, but the diurnal variation of albedo is more flat than that of the control, similar to the Amazon case. Overall, the daily averaged F_{ga} increases more than $10 W m^{-2}$, and corresponding F_{ca} and F_{sr} both decrease more than $5 W m^{-2}$.

For central Asia, the ground is sparsely vegetated, having a relatively small f_c value. The shadow effects increase F_{ca} and reduce F_{sr} and F_{ga}, especially for low sun. The differences for July are larger than that for January and can be more than $5 W m^{-2}$ in F_{ca} on average. The statistical results of three representative regions in the other months are given in Table 4.

3) SUNLIT–SHADED LAI AND ABSORPTION COMPARISON

The 3D model considers the overlapping of shadows between layers, which makes the P_{sun} less than 1 in the lower layers, decreasing the sunlit LAI (L_{sun}). Figure 11 shows the difference of L_{sun} for monthly-mean values over 3 years. The decrease in January happens mainly in the Southern Hemisphere with the area covered by multiple layers (Fig. 11a). In July, the area with decrease expands to the Northern Hemisphere, especially in the boreal region and eastern United States where multiple layers occur (Fig. 11b). However, the magnitude of the difference is mostly within $0.2 m^2 m^{-2}$.

The redistribution of absorbed diffuse radiation (section 4a) increases the sunlit canopy absorption. Together with the effects caused by the changing of L_{sun}, the differences of the total sunlit canopy absorption $F_{ca,sun}$ and total shaded canopy absorption $F_{ca,sha}$ are plotted in Fig. 11. The tropical area, with one layer and dense canopy cover, shows consistently decreased $F_{ca,sha}$ and increased $F_{ca,sun}$ for January and July. However, the decreased magnitude is much larger. In January, the boreal region at latitudes 50°–60°N gets a higher $F_{ca,sun}$. In July, the boreal region shows a large decrease of $F_{ca,sha}$. The $F_{ca,sun}$ increases mainly in areas with a one-layer dense canopy or sparsely vegetated cover. For areas covered by multiple layers, $F_{ca,sun}$ decreases slightly.

5. Discussion

In this study, a spherical bush is used as a building module to represent the canopy in a simple way. The maximum coverage of spheres of the same size without vertical projection overlapping could only be up to 90.69% if hexagonally close packed. If sphere sizes were variable, the coverage would be higher. To achieve even higher cover (i.e., near 100%), we can assume that the sphere has edges like the approximation of a regular hexagon to a circle. The random generation of a canopy scene of more than 80% coverage in a MC simulation

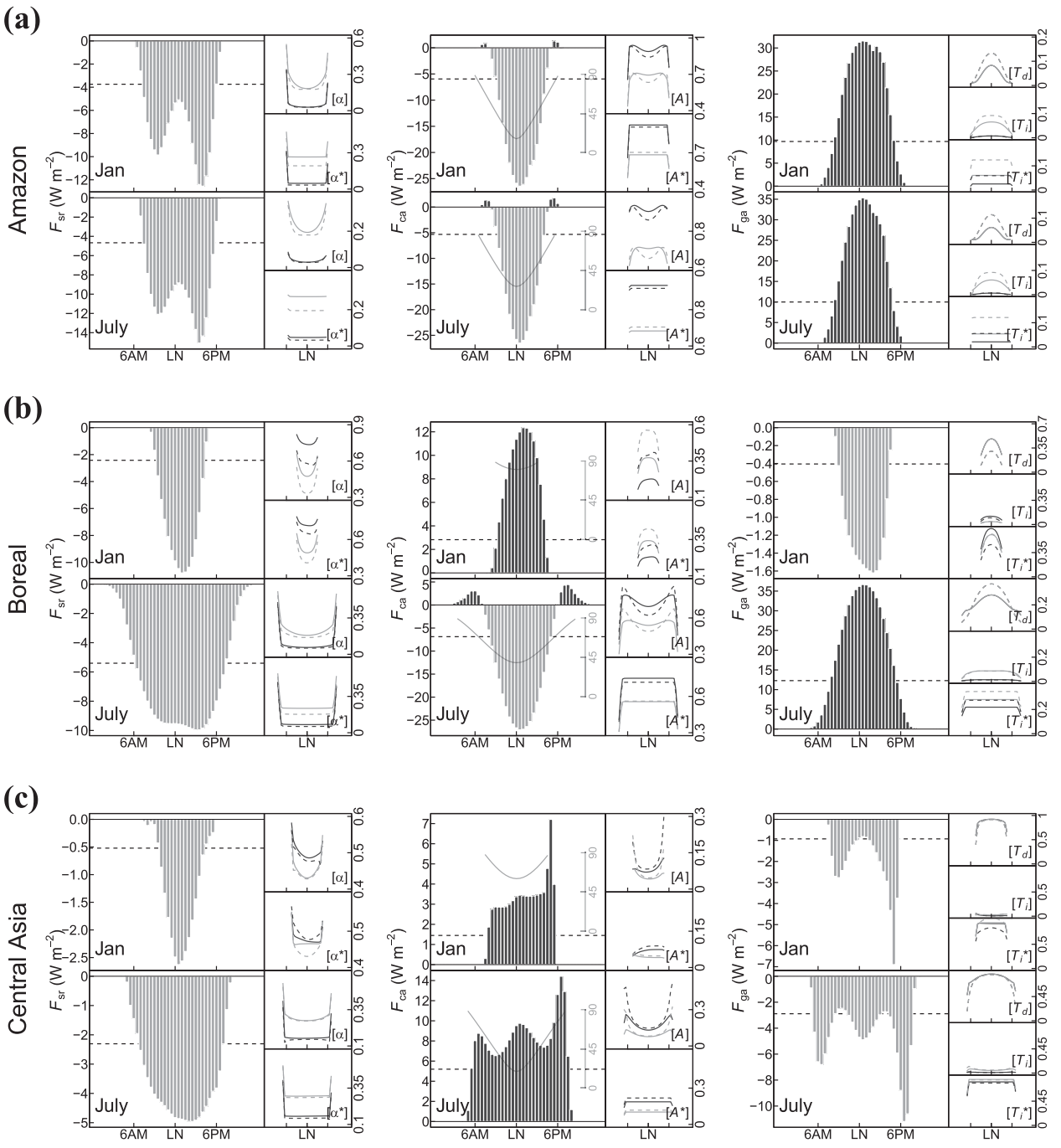

FIG. 10. Diurnal cycle comparison of surface solar radiation flux. The histograms from left to right F_{sr}, F_{ca}, and F_{ga} that are the difference between the 3D run and control run, and a dash line within is the mean difference and a solid line in the F_{ca} plot is the θ_{sun}. LN means local noontime: (a) the Amazon, (b) boreal, and (c) central Asia regions; and for each location the top panels are for January and the bottom, July. The smaller plots beside the histograms represent the components of albedo, canopy absorption, and transmission. The 3D result is plotted with a dashed line, and the two-stream model is a solid line. A dark line represents the VIS domain, and a gray line represents the NIR domain. The quantities [α] and [α*] stand for the albedo of incident direct and diffuse radiation, respectively. The quantities [A] and [A*] are the canopy absorption of incident direct and diffuse radiation, respectively. The quantity [T_d] is the direct transmission of incident direct radiation, [T_i] is the diffuse transmission of incident direct radiation, and [T_i^*] is the diffuse transmission of incident diffuse radiation.

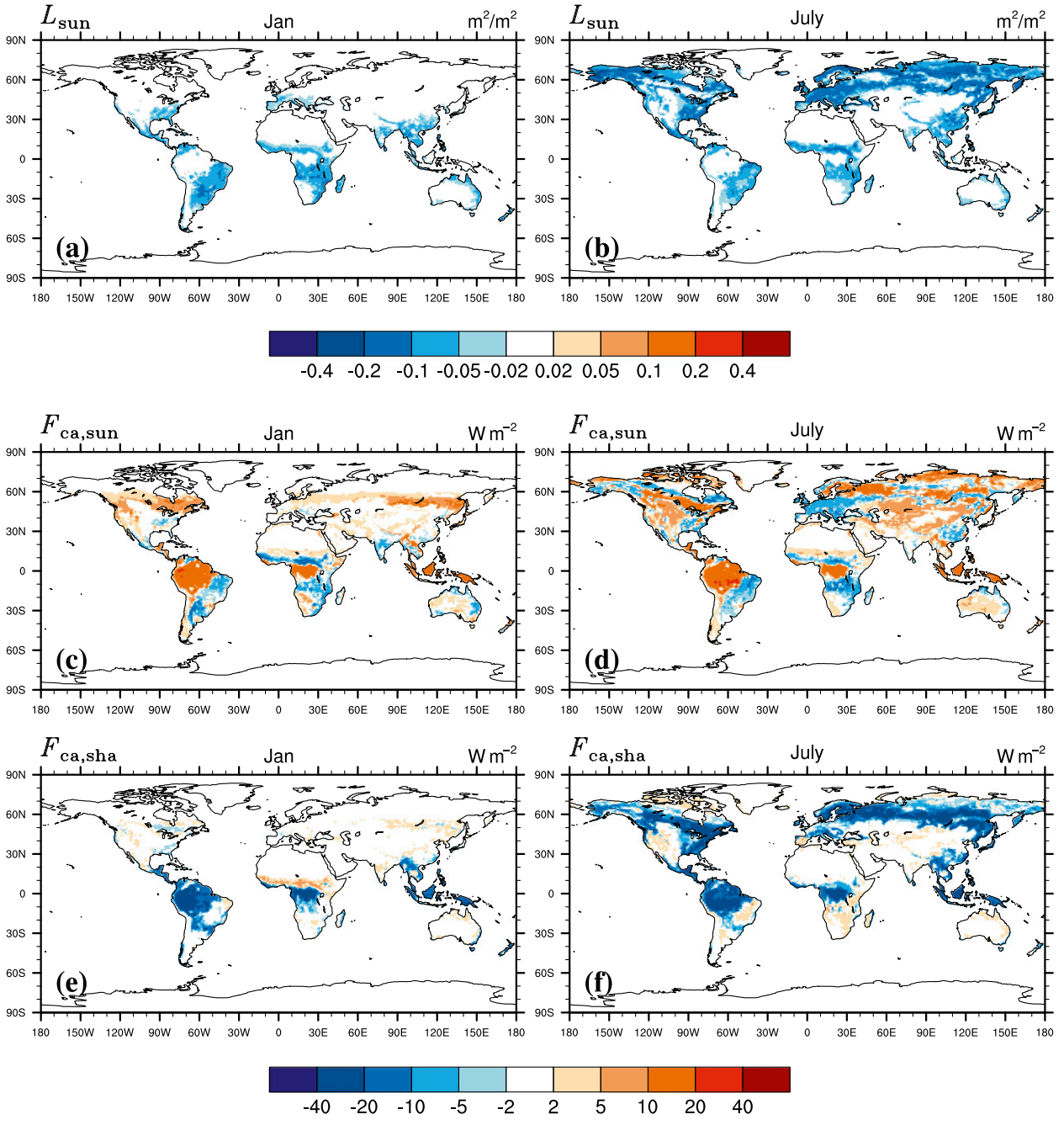

FIG. 11. The difference of sunlit–shaded LAI and canopy-absorbed radiation fluxes. (a),(b) L_{sun} is the sunlit LAI, (c),(d) $F_{ca,sun}$ is the total sunlit canopy-absorbed radiation flux, and (e),(f) $F_{ca,sha}$ is the total shaded canopy-absorbed radiation flux: (left) January and (right) July.

could easily fail without human intervention and was not implemented in this study. Each spherical bush of the same PFT is assumed to have the same LAI so that all bushes have the same τ_0 independent of their size. Thus, each bush has the same scattering properties so that we can conveniently apply the 3D model for one PFT with a single τ_0 parameter. In reality, LAIs of bushes may vary with bush sizes. However, if bushes have only small variations in size, the assumption of a single LAI is reasonable.

Spheres can be extended to ellipsoids through a simple linear transformation of one of its axes (Li and Strahler 1988). The effective θ_{sun} is correspondingly changed in the new coordinates, as well as the shadow calculations. Other distinctly different geometries, such as cones, would best be included by the summarization of numerical

computations, through fitting of other expressions, or by lookup tables. We use only a sphere here, not only due to its simplification, but also since observational data of canopy shape on a global scale are absent. Only a spherical LAD is considered in this study. Further refinements, such as allowing for differences in LAD, could be done. However, the daily average value of each radiation component would differ only slightly since it is an integral result over the entire day. We compared two control runs: one with such a LAD consideration and the other with just spherical LAD. The replotted Fig. 9 did not show any noticeable differences.

Besides the uncertainties inferred from the single bush calculations, a more important issue is the distribution of canopy crowns, which affects the shadow calculations, especially for nonclosed vegetation. In our study, without having information about the distribution of ground coverage, all PFTs are assumed to have a horizontally random distribution without the overlap of vertical projections and collocate (mix) within the grid. Individual trees or bushes locate themselves within a forest according to random choices and optimization principles (e.g., they may prefer to distance themselves to some extent from rivals because of competition for light, nutrients, and water). The absence of vertical projection overlapping is also consistent with the vegetation in CLM4.0 that are all determined based on the PFT levels without vertical overlapping, as is the input land surface data. In reality, overlap of vertical projections between PFTs could exist (e.g., to form an understory layer). In this case, the total canopy f_c may exceed 100%, such as in the Amazon. To apply the 3D model, the calculations of overlapped shadow between layers could be revised to be randomly overlapping with the constraint of self-area shadow removed. In addition, different PFTs may prefer not to collocate but be separate, such as in Arctic, where because of shortage of cold and light, it may be difficult to support more than a one layer canopy. The 3D model could be further improved with more details of canopy layer information, which could be retrieved by spaceborne lidar data (van Leeuwen and Nieuwenhuis 2010) or supplied by the prognostic variables from dynamic vegetation models.

In atmospheric radiative transfer, the equivalent angle for incident isotropic diffuse radiation has commonly been assumed to be 52.96 based on the diffusivity factor $D = 1.66$ (Elsasser 1942). The term D is an approximation for the equivalent average pathlength for the diffuse transmission (uncollided) function calculation; that is, using $\exp(-D\tau')$ to approximate $2\int_0^1 \exp(-\tau'/\mu)\mu\, d\mu$, τ' is the total optical depth along the shortest path (vertical). However, D depends on τ' such that for $\tau' \to 0$, $D \to 2$ (equivalent angle = 60°) and $\tau' \to \infty$, $D \to 1$ (0°). For a canopy, D also depends on LAD, as well as canopy crown shapes, spatial distribution, and f_c in a 3D scene. For spherical bushes with small f_c in a random distribution, $D \to 2$ (especially for a single bush, $D = 2$ for all τ_0). For a large canopy cover (e.g., 100% coverage of a 1D canopy with spherical LAD), we compared different D values in the diffuse transmission function calculation in Fig. 12: $D = 2$ is currently used in CLM4.0 and 4.5 and $D = 1.41$ (0.705/0.5) is suggested by Pinty et al. (2006). For the 3D model, D was chosen as 2 but applied in the 3D direct transmission calculation scheme. Figure 12 shows that the 3D model performs similarly to the 1D model with $D = 1.66$, and better than 1D model with $D = 2$, but still underestimates the diffuse transmission at intermediate LAI values. A slight decrease of D in the 3D model would give a better match with the numerical simulations under these conditions. In this study, for comparison, we made the same assumption as CLM 4.0 and 4.5 with $D = 2$ (60°) for the canopy with a spherical LAD.

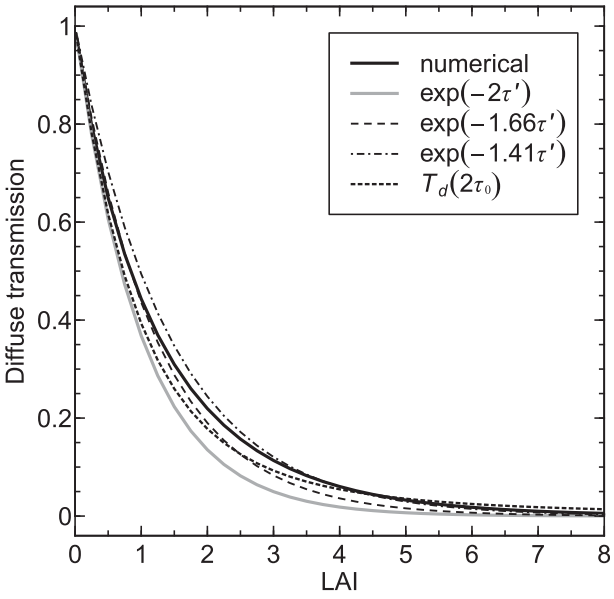

FIG. 12. Comparison of different diffusivity factors for approximating the diffuse transmission $2\int_0^1 \exp(-\tau'/\mu)\mu\, d\mu$ (calculated by numerical integration) for a 1D canopy with spherical LAD. The notation exp(·) in the legend represents the 1D model, $T_d(\cdot)$ is the 3D model when $f_c = 100\%$, and the numbers in the parentheses are the diffusivity factors. The value τ' is calculated as (½)LAI, and τ_0 is calculated as (⅜)LAI.

The canopy 3D structures considered in the model, such as its crown shape, horizontal distribution, and vertical layering, are appropriate for leaves clumping at the canopy (i.e., crown) level. We have not taken into account the heterogeneities within a crown, such as the vertical leaf density profile and the leaves clumping at

shoot level. Another issue not considered yet is the interactions of canopy radiation with topography, which could be important in a mountainous area.

The dependence on θ_{sun} of albedo is complicated, as summarized by Dickinson (1983). Albedo commonly increases with increasing θ_{sun}. However, Oleson et al. (2003) and Wang et al. (2004) found that the albedo calculated by the two-stream model in CLM2.0 increases more rapidly with θ_{sun} than the MODIS data. The diagnosed variation of Wang et al. (2004) has a similar slope but is flatter for the MODIS data than for the two-stream model. Their conclusion is consistent with our diurnal comparison in the Amazon and boreal region in a snow-free season (Figs. 10a,b). Soil albedo is important to the total surface albedo, especially in a sparsely vegetated area or with small LAI. One noticeable issue is that the soil albedo represented in the current CLM4.0 is independent of θ_{sun}. However, the observational MODIS data show a dependence on θ_{sun} (Wang et al. 2004) that may contribute to the increase of albedo with large θ_{sun} and so would lead to an even larger increase of albedo in the two-stream model. In a sparsely vegetated area, such as central Asia, Sahel, and the central United States, without considering this soil albedo variation, the 3D model actually shows a slight decrease with the increase of θ_{sun} in the VIS domain (as shown in Fig. 10c) due to the 3D shadow effects. Soil albedo can be adjusted through a fitting with the MODIS albedo data in order to get a better match (Lawrence and Chase 2007). However, an inclusion of the sun angle dependence of soil albedo could further improve CLM's matching to observed surface albedo.

Further direct validations against observations are still needed in the future. MODIS albedo products (Schaaf et al. 2002) can be used to validate the model's output of albedo. A comparison of zonal average albedo (at LN) from the control run, 3D run, and MODIS is shown in Fig. 13. MODIS data were aggregated from MODIS MCD43C3 products to the model output resolution in this study. The averages of year 2001–03 for both model outputs and MODIS data were compared. Only the grids with land fraction $\geq$99% and lake fraction $<$20% were included in the comparison to avoid the ocean and lake effects (Oleson et al. 2003). All sky albedo of MODIS are composited by VIS and NIR: black-sky (direct) and white-sky (diffuse) albedo weighted by the fraction of radiation fluxes in corresponding regimes the same as the model. In general, the 3D model shows a similar performance as the two-stream model. It seems that the 3D model may have some improvements at latitudes 50°–60°N in December–February (DJF) and partly improve the performance of the white-sky albedo simulation (more noticeable in NIR domain). The control run does not always overestimate the NIR white-sky albedo caused by the overestimation of albedo with θ_{sun} in the two-stream model as expected. It agrees well with MODIS NIR white-sky albedo at latitudes 5°–30°S in DJF and at latitudes 40°–60°N in June–August (JJA). Both two-stream and 3D models underestimate the NIR black-sky albedo at latitudes 0°–20°S in DJF and at latitudes 0°–10°N and 50°–60°N in JJA. The larger, even opposite variation of MODIS NIR black- and white-sky albedo (Figs. 13d,e,i,j) cannot be explained by the change of LAI, θ_{sun}, and r_g. This indicates some other factors may affect the canopy's albedo. A possible reason could be the variation of leaf optical properties (prescribed as constants in the model) caused by the change of leaf water content or leaf tissue structure. The model's albedo is highly dependent on the input datasets (e.g., LAI, leaf optical properties, r_g, and snow fraction). It is important to identify the source of the bias, whether it is from the model structure, the input datasets or possibly the observation itself. The global fraction of absorbed photosynthetically active radiation (fAPAR) datasets, for example, MODIS (Myneni et al. 2002), Carbon Cycle and Change in Land Observational Products from an Ensemble of Satellites (CYCLOPES) (Baret et al. 2007), Joint Research Center (JRC) (Gobron et al. 2006), and Global Land Products for Carbon Model Assimilation (GLOBCARBON) (Plummer et al. 2007), could be used to validate the model canopy absorption in the VIS domain. However, large discrepancies may exist among these datasets due to the differences of satellite passing time, the definition of fAPAR values calculated, statistical methods, input datasets for retrieval algorithms, and the radiative assumptions (Weiss et al. 2007; McCallum et al. 2010; Wang et al. 2013). These discrepancies may even exceed the differences between two-stream and 3D models. Careful examination of the fAPAR datasets is required in comparing the model and satellite retrieval data. Site level validation could be done using the FLUXNET datasets (Baldocchi et al. 2001) in the presence of known canopy structure (e.g., layers information and crown density) and measurements related to the radiation fluxes.

6. Conclusions

The 1D canopy radiative transfer models used in climate modeling, such as the two-stream model, are unrealistic in their assumption of a homogeneous canopy. To consider the 3D structure of a canopy in terms of its crown shape, horizontal distribution, and vertical levels, a new 3D model parameterization has been developed. The individual elements of the 3D model are modularized. A one-layer model was constructed by

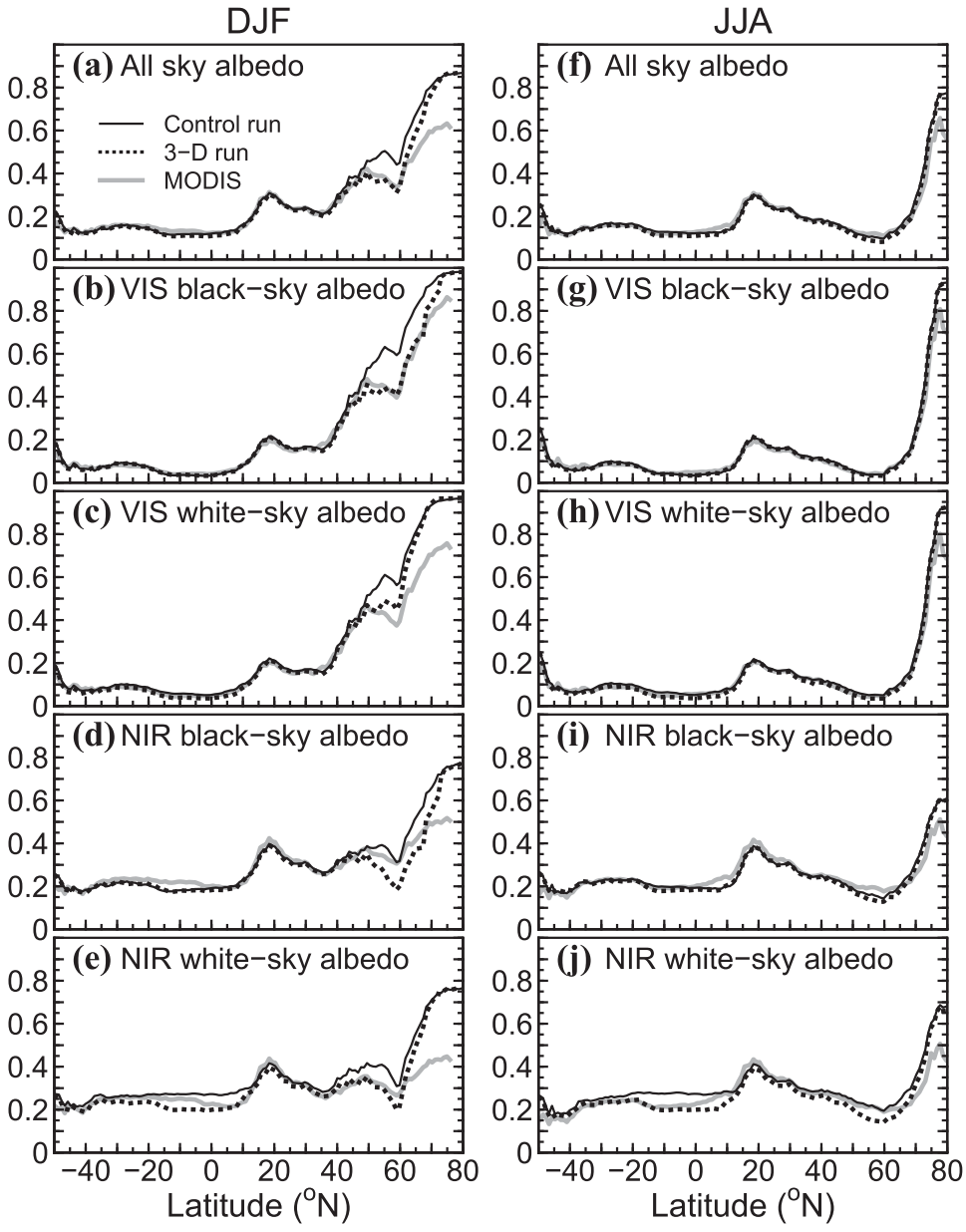

FIG. 13. Zonal averages of albedo at local noon for control run, 3D run, and MODIS: (left) DJF and (right) JJA and albedos for (a),(f) all-sky, (b),(g) VIS black-sky, (c),(h) VIS white-sky, (d),(i) NIR black-sky, and (e),(j) NIR white-sky conditions.

combining single bush models taking into account effects of their shadows, intercanopy interactions, and low sun angles. The one-layer model was used to build up the three-layer model by considering the shadow overlapping between layers. The 3D model so developed is simple and effective and is in good agreement with numerical simulations. We implemented the 3D model into the land component of a climate model, CLM4.0, and compared it with the default two-stream model. The results show that canopy absorption increases primarily in sparsely vegetated areas and for multiple-layered areas with large θ_{sun} and is the result of increases of the ground and sky shadows and of the optical pathlength because of the shadow overlapping between bushes and layers. Decreases happen primarily in densely vegetated areas with small θ_{sun}. For a one-layer canopy, heterogeneous pathlength effects increase the transmission through the canopy edge and so decrease the canopy absorption (e.g., tropical forest areas have a decrease of about $6\,W\,m^{-2}$ throughout the year). For

a multilayer canopy, in addition to these shape effects, the decreased total ground shadow due to its overlapping between layers also increases the transmittance; for example, the boreal region in summer correspondingly decreases by about $6\,W\,m^{-2}$ in its canopy absorption. Ground absorption usually shows an opposite change to that of canopy absorption. Over all land, it has higher values throughout the year with the 3D model, especially in summer ($>5\,W\,m^{-2}$). The largest contributions come from the boreal region ($\sim 11\,W\,m^{-2}$). Dense vegetation in the tropics also contributes throughout the year ($\sim 10\,W\,m^{-2}$). Slight decreases happen in the most sparsely vegetated areas throughout the year and also in the boreal region in January–April. The 3D model gives slightly lower albedo over most vegetated areas throughout the year, especially in the boreal region in early spring (flux up to $-9\,W\,m^{-2}$), and the corresponding canopy absorption substantially increases ($\sim 10\,W\,m^{-2}$). The 3D model also affects the sunlit/shaded LAI and corresponding absorption. Further improvements and refinements could be made with the help of more details provided by observational data as model constraints. Nevertheless, the 3D model now provides a much more realistic treatment of terrestrial canopy radiation for use in climate modeling and evaluation by the community.

Acknowledgments. This work was supported by Office of Science (BER) DOE Grant DE-FG02-09ER64746, the program of the Intellectual Introduction Project for the Discipline Innovation in China University System (111 Program), the Natural Science Foundation of China (under Grant 40875062), and the R&D Special Fund for Nonprofit Industry of China (Meteorology GYHY200706025). Dr. Xiaowen Li is thanked for some helpful insights provided at the initial stages of this research. We thank two anonymous reviewers for their thorough and constructive review. Thanks to Jamie Wentz and Jeffrey Hopkins for assistance with the word processing.

APPENDIX A

Single Bush Model

Dickinson et al. (2008) and Dickinson (2008) developed a single bush model with its basic assumptions (section 2a). With overhead sun ($\theta_{sun} = 0°$, $\mu = \cos\theta_{sun} = 1$) and isotropic leaf scattering, the model calculates the direct transmission by integrating over all realized path lengths as

$$T_{d,s}(\tau) = 0.5\tau^{-2}[1 - (1 + 2\tau)e^{-2\tau}]. \quad \text{(A1)}$$

Incident direct radiation, first colliding with leaves, can scatter backward or forward out of canopy as illustrated as Part I in Fig. A1a giving the first-order backward-scattering phase function Φ_{1b} and first-order forward-scattering phase function Φ_{1f}:

$$\Phi_{1b}(\tau) = 0.5[1 - T_{d,s}(2\tau)] \quad \text{(A2)}$$

and

$$\Phi_{1f}(\tau) = \tau^{-2}[1 - (1 + 2\tau + 2\tau^2)e^{-2\tau}], \quad \text{(A3)}$$

where Φ_{1b} and Φ_{1f} are normalized by dividing by $0.25\omega/\pi$. After the first scattering, the radiation, which has been passed though optical pathlength h' as the dashed circle point (Part II, Fig. A1a), can scatter again with leaves at the solid circle point h. The diffuse pathlength, which from all possible points with length h' to h was approximated as that of the infinite parallel plane of the 1D case, which is $-2|h - h'|$, and the proportion of radiation scattered to h are evaluated as $\tau e^{-2\tau|h-h'|}$. Using numerical fitting to improve the results of Dickinson (2008), we replaced this term by $a\tau e^{-b\tau|h-h'|}$ instead of $\tau e^{-2\tau|h-h'|}$, where $a = 0.70$ and $b = 1.74$ are parameters chosen to match numerical simulation results. The radiation to point h, just as the first-order case, can be either scattered backward or forward out of the canopy as the second-order backward-scattering phase function Φ_{2b} and second-order forward-scattering phase function Φ_{2f} from which the integration is

$$\Phi_{2b}(\tau) = a\left\{\frac{1}{b+1} - \frac{1}{b-1}T_{d,s}(2\tau) + \frac{2}{(b+1)(b-1)}T_{d,s}[(b+1)\tau]\right\} \quad \text{(A4)}$$

and

$$\Phi_{2f}(\tau) = a\left\{\frac{2b}{b^2-1}\Phi_{1f}(\tau) - \left[\frac{1}{(b+1)^2} + \frac{1}{(b-1)^2}\right]T_{d,s}(\tau) + \frac{1}{(b-1)^2}T_{d,s}(b\tau) + \frac{1}{(b+1)^2}T_{d,s}[(b+2)\tau]\right\}, \quad \text{(A5)}$$

where Φ_{2b} and Φ_{2f} are normalized by dividing by $0.25\omega^2/\pi$. For $a = 1$ and $b = 2$, Eqs. (A4) and (A5) are the same as the Eqs. (19) and (20) in Dickinson (2008). Assuming each order-scattering phase function changes linearly from the backward to forward direction, the total first- and second-order scattering are simply

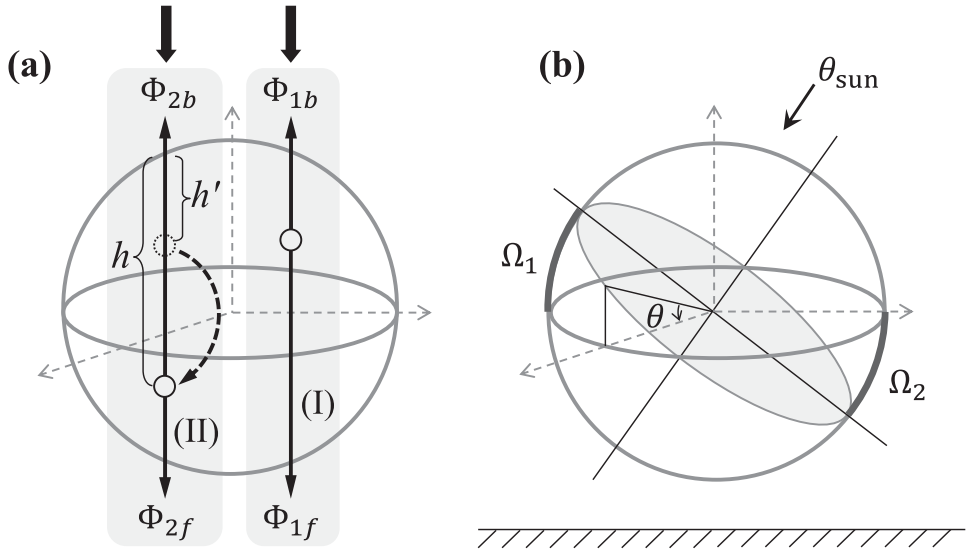

FIG. A1. Sketches of the single bush model calculation.

$$\Phi_{1a}(\tau) = 0.5[\Phi_{1b}(\tau) + \Phi_{1f}(\tau)] \tag{A6}$$

and

$$\Phi_{2a}(\tau) = 0.5[\Phi_{2b}(\tau) + \Phi_{2f}(\tau)], \tag{A7}$$

respectively. The recollision probability (Panferov et al. 2001; Smolander and Stenberg 2005), after the second-order scattering, can be calculated as

$$p_2(\tau) = 1 - \frac{\Phi_{2a}(\tau)}{1 - T_{d,s}(\tau) - \Phi_{1a}(\tau)}. \tag{A8}$$

The third- and higher-order scattering phase functions are assumed isotropic. Using the recollision probability concept gives the third- and higher-order scattering phase functions as

$$\Phi_{3+}(\tau) = \frac{\omega p_2(\tau)\Phi_{2a}(\tau)}{1 - \omega p_2(\tau)}; \tag{A9}$$

Φ_{3+} is also normalized by dividing by $0.25\omega^2/\pi$.

The total backward- and forward-scattering phase functions are then constructed as

$$\Phi_b(\tau) = \frac{\omega}{4\pi}\Phi_{1b}(\tau) + \frac{\omega^2}{4\pi}[\Phi_{2b}(\tau) + \Phi_{3+}(\tau)] \tag{A10}$$

and

$$\Phi_f(\tau) = \frac{\omega}{4\pi}\Phi_{1f}(\tau) + \frac{\omega^2}{4\pi}[\Phi_{2f}(\tau) + \Phi_{3+}(\tau)]. \tag{A11}$$

For bi-Lambertian leaf scattering, only the first-order backward- and forward-scattering phase functions are modified by multiplying the factors $2r/\omega$ and $2t/\omega$, respectively. We still assume the phase function to vary linearly from the backward to forward direction. Then the phase function with an out-scattering angle θ_{out} ($\mu_{\text{out}} = \cos\theta_{\text{out}}$) is calculated as

$$\Phi_{\mu_{\text{out}}}(\tau) = \Phi_a(\tau) + \mu_{\text{out}}\Phi_d(\tau), \tag{A12}$$

where $\Phi_a(\tau) = 0.5[\Phi_b(\tau) + \Phi_f(\tau)]$ and $\Phi_d(\tau) = 0.5[\Phi_b(\tau) - \Phi_f(\tau)]$. The albedo can be simply integrated as $\alpha_s(\mu = 1, \tau) = 2\pi[\Phi_a(\tau) + 0.5\Phi_d(\tau)]$, and diffuse transmission is $T_{i,s}(\mu = 1, \tau) = 2\pi[\Phi_a(\tau) - 0.5\Phi_d(\tau)]$. For the sun at a θ_{sun} ($\mu = \cos\theta_{\text{sun}}$), as illustrated in Fig. A1b, the overhead sun case is modified by accounting for one sector (Ω_1, downward in overhead sun case) that added to albedo and one sector (Ω_2, upward in overhead sun case) that subtracted. With these complications, the albedo is derived as

$$\alpha_s(\mu, \tau) = \alpha_s(\mu = 1, \tau) + \int_{\Omega_1}\left[\Phi_a + \cos\left(\frac{\pi}{2} + \theta\right)\Phi_d\right]d\Omega - \int_{\Omega_2}\left[\Phi_a + \cos\left(\frac{\pi}{2} - \theta\right)\Phi_d\right]d\Omega. \tag{A13}$$

The last two items are combined and calculated as

$$\int_{\Omega_1(\Omega_2)} -2\sin\theta\Phi_d\, d\Omega = -\pi(1 - \mu)\Phi_d. \tag{A14}$$

Note that the upper limit of θ on the left side in Eq. (A14) is depended on the azimuth angle, and its

integration was derived in detail by Norman and Jarvis (1975, their appendix A). The diffuse transmission can be derived in the same way. The albedo and diffuse transmission for a single bush are thus calculated as

$$\alpha_s(\mu,\tau) = 2\pi[\Phi_a(\tau) + 0.5\mu\Phi_d(\tau)] \qquad \text{(A15)}$$

and

$$T_{i,s}(\mu,\tau) = 2\pi[\Phi_a(\tau) - 0.5\mu\Phi_d(\tau)]. \qquad \text{(A16)}$$

APPENDIX B

Intercanopy Interactions

The distance between bushes has been assumed random for shadow calculations. However, for close spacing, ecological reasoning suggests spacing likely to be more uniform. To determine intercanopy interactions we simply assume that the canopy distribution is hexagonally arranged (Fig. B1a) and that the intercanopy interaction effect is independent of θ_{sun}. The view factor V_1 for the central ball to its one of the nearest balls in distance L_1 (Fig. B1b) is

$$V_1 = \frac{1}{2}(1 - \cos\theta_v) = \frac{1}{2}\left[1 - \sqrt{1 - \left(\frac{R}{L_1}\right)^2}\right], \qquad \text{(B1)}$$

where

$$\left(\frac{R}{L_1}\right)^2 = \frac{\sqrt{3}f_c}{2\pi}. \qquad \text{(B2)}$$

Six balls are so arranged and further six balls at distance L_2 are also accounted for. The total view factor V is then

$$V = 6V_1 + 6V_2 = 3\left[1 - \sqrt{1 - \frac{\sqrt{3}f_c}{2\pi}}\right] + 3\left[1 - \sqrt{1 - \frac{\sqrt{3}f_c}{6\pi}}\right]. \qquad \text{(B3)}$$

We assume V is in the middle of a sphere with a uniform distribution in the azimuth angle (Fig. B1c). The initial intercepted radiation is the integration of single bush scattering phase function ($\theta_{\text{sun}} = 0°$) within V, which is $4\pi V\Phi_a(\tau_0)$. Then we use the recollision probability concept [p_2 denotes the recollision probability calculated by Eq. (A8)] to calculate the total absorbed radiation due to intercanopy interactions as

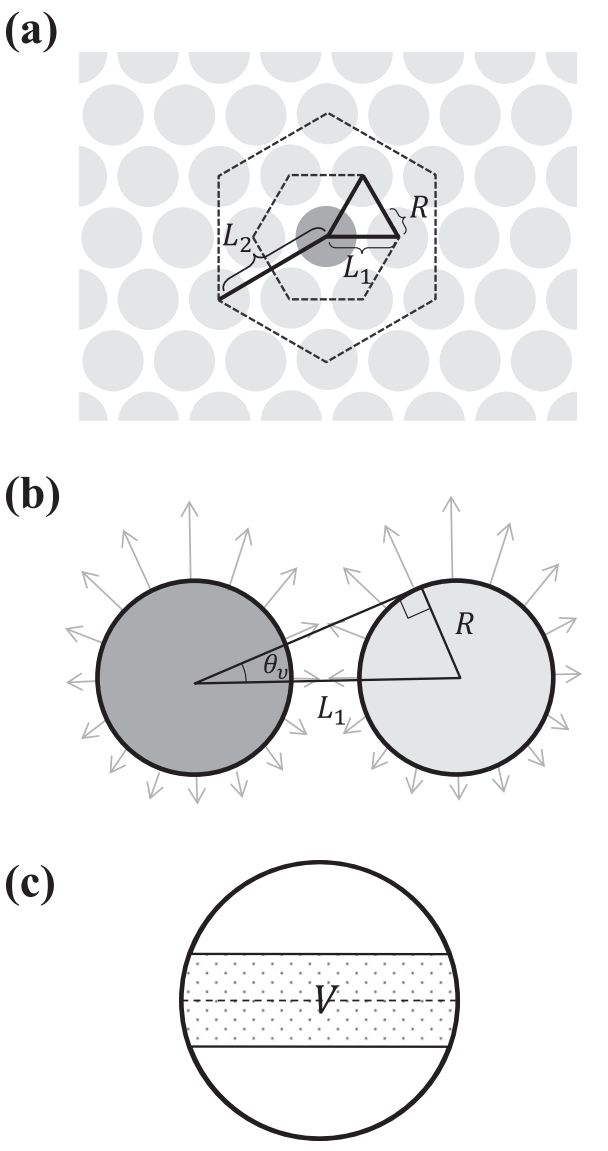

FIG. B1. Sketches of the intercanopy interaction calculation.

$$A_c = 4\pi V\Phi_a(\tau_0)[1 - T_{d,s}(\tau_0)]\frac{1-\omega}{1-\omega p_2(\tau_0)}. \qquad \text{(B4)}$$

APPENDIX C

Self-Area Shadow Calculation

Li and Strahler (1992) gave the solution for calculating the overlapping area between shadows generated from direct illumination and view angle (view shadow). Self-area shadow is the simplest case when the view angle is vertically downward. Vertical projection is then equivalent to the view shadow. The self-area shadow is simply

$$R^2(t - \cos t \sin t)(1 + \sec\theta_{\text{sun}}), \tag{C1}$$

where

$$t = \cos^{-1}\left[\frac{h\tan\theta_{\text{sun}}}{R(1 + \sec\theta_{\text{sun}})}\right]. \tag{C2}$$

The R in Eqs. (C1) and (C2) is the radius of bush, and h is the height from the crown central point to a reference height level.

REFERENCES

Baldocchi, D., and Coauthors, 2001: FLUXNET: A new tool to study the temporal and spatial variability of ecosystem–scale carbon dioxide, water vapor, and energy flux densities. *Bull. Amer. Meteor. Soc.,* **82,** 2415–2434.

Baret, F., and Coauthors, 2007: LAI, fAPAR and fCover CYCLOPES global products derived from VEGETATION: Part 1: Principles of the algorithm. *Remote Sens. Environ.,* **110,** 275–286, doi:10.1016/j.rse.2007.02.018.

Bonan, G. B., 1996: A land surface model (LSM version 1.0) for ecological, hydrological, and atmospheric studies: Technical description and user's guide. NCAR Tech. Note NCAR/TN-417+STR, 150 pp.

——, P. J. Lawrence, K. W. Oleson, S. Levis, M. Jung, M. Reichstein, D. M. Lawrence, and S. C. Swenson, 2011: Improving canopy processes in the Community Land Model version 4 (CLM4) using global flux fields empirically inferred from FLUXNET data. *J. Geophys. Res.,* **116,** G02014, doi:10.1029/2010JG001593.

Chen, J. M., and T. A. Black, 1991: Measuring leaf area index of plant canopies with branch architecture. *Agric. For. Meteor.,* **57,** 1–12, doi:10.1016/0168-1923(91)90074-Z.

Dai, Y., R. E. Dickinson, and Y.-P. Wang, 2004: A two-big-leaf model for canopy temperature, photosynthesis, and stomatal conductance. *J. Climate,* **17,** 2281–2299.

Dickinson, R. E., 1983: Land surface processes and climate—Surface albedos and energy balance. *Advances in Geophysics,* Vol. 25, Academic Press, 305–353.

——, 2008: Determination of the multi-scattered solar radiation from a leaf canopy for use in climate models. *J. Comput. Phys.,* **227,** 3667–3677, doi:10.1016/j.jcp.2007.12.010.

——, A. Henderson-Sellers, P. J. Kennedy, and M. F. Wilson, 1986: Biosphere Atmosphere Transfer Scheme (BATS) for the NCAR community climate model. NCAR Tech. Note NCAR/TN-275+STR, 66 pp.

——, L. Zhou, Y. Tian, Q. Liu, T. Lavergne, B. Pinty, C. B. Schaaf, and Y. Knyazikhin, 2008: A three-dimensional analytic model for the scattering of a spherical bush. *J. Geophys. Res.,* **113,** D20113, doi:10.1029/2007JD009564.

Elsasser, W. M., 1942: *Heat Transfer by Infrared Radiation in the Atmosphere.* Vol. 6. Harvard University Press, 87 pp.

Gobron, N., and Coauthors, 2006: Evaluation of fraction of absorbed photosynthetically active radiation products for different canopy radiation transfer regimes: Methodology and results using Joint Research Center products derived from SeaWiFS against ground-based estimations. *J. Geophys. Res.,* **111,** D13110, doi:10.1029/2005JD006511.

Hansen, M. C., R. S. DeFries, J. R. G. Townshend, M. Carroll, C. Dimiceli, and R. A. Sohlberg, 2003: Global percent tree cover at a spatial resolution of 500 meters: First results of the MODIS vegetation continuous fields algorithm. *Earth Interact.,* **7,** doi:10.1175/1087-3562(2003)007<0001:GPTCAA>2.0.CO;2.

Knyazikhin, Y., J. V. Martonchik, R. B. Myneni, D. J. Diner, and S. W. Running, 1998: Synergistic algorithm for estimating vegetation canopy leaf area index and fraction of absorbed photosynthetically active radiation from MODIS and MISR data. *J. Geophys. Res.,* **103** (D24), 32 257–32 276, doi:10.1029/98JD02462.

Lawrence, P. J., and T. N. Chase, 2007: Representing a new MODIS consistent land surface in the Community Land Model (CLM 3.0). *J. Geophys. Res.,* **112,** G01023, doi:10.1029/2006JG000168.

Li, X., and A. H. Strahler, 1985: Geometric-optical modeling of a conifer forest canopy. *IEEE Trans. Geosci. Remote Sens.,* **GE-23,** 705–721, doi:10.1109/TGRS.1985.289389.

——, and ——, 1988: Modeling the gap probability of a discontinuous vegetation canopy. *IEEE Trans. Geosci. Remote Sens.,* **26,** 161–170, doi:10.1109/36.3017.

——, and ——, 1992: Geometric-optical bidirectional reflectance modeling of the discrete crown vegetation canopy: Effect of crown shape and mutual shadowing. *IEEE Trans. Geosci. Remote Sens.,* **30,** 276–292, doi:10.1109/36.134078.

——, ——, and C. E. Woodcock, 1995: A hybrid geometric optical-radiative transfer approach for modeling albedo and directional reflectance of discontinuous canopies. *IEEE Trans. Geosci. Remote Sens.,* **33,** 466–480, doi:10.1109/36.377947.

McCallum, I., W. Wagner, C. Schmullius, A. Shvidenko, M. Obersteiner, S. Fritz, and S. Nilsson, 2010: Comparison of four global FAPAR datasets over northern Eurasia for the year 2000. *Remote Sens. Environ.,* **114,** 941–949, doi:10.1016/j.rse.2009.12.009.

Myneni, R. B., and Coauthors, 2002: Global products of vegetation leaf area and fraction absorbed PAR from year one of MODIS data. *Remote Sens. Environ.,* **83,** 214–231, doi:10.1016/S0034-4257(02)00074-3.

Nilson, T., 1971: A theoretical analysis of the frequency of gaps in plant stands. *Agric. Meteor.,* **8,** 25–38, doi:10.1016/0002-1571(71)90092-6.

Ni-Meister, W., W. Yang, and N. Y. Kiang, 2010: A clumped-foliage canopy radiative transfer model for a global dynamic terrestrial ecosystem model. I: Theory. *Agric. For. Meteor.,* **150,** 881–894, doi:10.1016/j.agrformet.2010.02.009.

Norman, J. M., and P. G. Jarvis, 1975: Photosynthesis in Sitka spruce (Picea sitchensis (Bong.) Carr.): V. Radiation penetration theory and a test case. *J. Appl. Ecol.,* **12,** 839–878.

——, and J. M. Welles, 1983: Radiative transfer in an array of canopies. *Agron. J.,* **75,** 481–488, doi:10.2134/agronj1983.00021962007500030016x.

North, P. R. J., 1996: Three-dimensional forest light interaction model using a Monte Carlo method. *IEEE Trans. Geosci. Remote Sens.,* **34,** 946–956, doi:10.1109/36.508411.

Oleson, K. W., G. B. Bonan, C. Schaaf, F. Gao, Y. Jin, and A. Strahler, 2003: Assessment of global climate model land surface albedo using MODIS data. *Geophys. Res. Lett.,* **30,** 1443, doi:10.1029/2002GL016749.

——, and Coauthors, 2010: Technical description of version 4.0 of the Community Land Model (CLM). NCAR Tech. Note NCAR/TN-478+STR, 257 pp.

Panferov, O., Y. Knyazikhin, R. B. Myneni, J. Szarzynski, S. Engwald, K. G. Schnitzler, and G. Gravenhorst, 2001: The role of canopy structure in the spectral variation of transmission and absorption

of solar radiation in vegetation canopies. *IEEE Trans. Geosci. Remote Sens.,* **39,** 241–253, doi:10.1109/36.905232.

Pinty, B., and Coauthors, 2001: Radiation Transfer Model Intercomparison (RAMI) exercise. *J. Geophys. Res.,* **106** (D11), 11 937–11 956.

——, N. Gobron, J.-L. Widlowski, T. Lavergne, and M. M. Verstraete, 2004a: Synergy between 1-D and 3-D radiation transfer models to retrieve vegetation canopy properties from remote sensing data. *J. Geophys. Res.,* **109,** D21205, doi:10.1029/2004JD005214.

——, and Coauthors, 2004b: Radiation Transfer Model Intercomparison (RAMI) exercise: Results from the second phase. *J. Geophys. Res.,* **109,** D06210, doi:10.1029/2003JD004252.

——, T. Lavergne, R. E. Dickinson, J.-L. Widlowski, N. Gobron, and M. M. Verstraete, 2006: Simplifying the interaction of land surfaces with radiation for relating remote sensing products to climate models. *J. Geophys. Res.,* **111,** D02116, doi:10.1029/2005JD005952.

Plummer, S., and Coauthors, 2007: An update on the globcarbon initiative: Multi-sensor estimation of global biophysical products for global terrestrial carbon studies. *Proc. ENVISAT Symp. 2007,* Montreux, Switzerland, European Space Agency, 23–27.

Qian, T., A. Dai, K. E. Trenberth, and K. W. Oleson, 2006: Simulation of global land surface conditions from 1948 to 2004. Part I: Forcing data and evaluations. *J. Hydrometeor.,* **7,** 953–975.

Schaaf, C. B., and Coauthors, 2002: First operational BRDF, albedo nadir reflectance products from MODIS. *Remote Sens. Environ.,* **83,** 135–148, doi:10.1016/S0034-4257(02)00091-3.

Sellers, P. J., 1985: Canopy reflectance, photosynthesis and transpiration. *Int. J. Remote Sens.,* **6,** 1335–1372, doi:10.1080/01431168508948283.

——, and Coauthors, 1996: A revised land surface parameterization (SiB2) for atmospheric GCMS. Part I: Model formulation. *J. Climate,* **9,** 676–705.

Smolander, S., and P. Stenberg, 2005: Simple parameterizations of the radiation budget of uniform broadleaved and coniferous canopies. *Remote Sens. Environ.,* **94,** 355–363, doi:10.1016/j.rse.2004.10.010.

van Leeuwen, M., and M. Nieuwenhuis, 2010: Retrieval of forest structural parameters using LiDAR remote sensing. *Eur. J. For. Res.,* **129,** 749–770, doi:10.1007/s10342-010-0381-4.

Wang, K., J. Mao, R. Dickinson, X. Shi, W. Post, Z. Zhu, and R. Myneni, 2013: Evaluation of CLM4 solar radiation partitioning scheme using remote sensing and site level FPAR datasets. *Remote Sens.,* **5,** 2857–2882, doi:10.3390/rs5062857.

Wang, S., 2005: Dynamics of surface albedo of a boreal forest and its simulation. *Ecol. Modell.,* **183,** 477–494, doi:10.1016/j.ecolmodel.2004.10.001.

Wang, Y.-P., 2003: A comparison of three different canopy radiation models commonly used in plant modelling. *Funct. Plant Biol.,* **30,** 143–152, doi:10.1071/FP02117.

Wang, Z., X. Zeng, M. Barlage, R. E. Dickinson, F. Gao, and C. B. Schaaf, 2004: Using MODIS BRDF and albedo data to evaluate global model land surface albedo. *J. Hydrometeor.,* **5,** 3–14.

Weiss, M., F. Baret, S. Garrigues, and R. Lacaze, 2007: LAI and fAPAR CYCLOPES global products derived from VEGETATION. Part 2: Validation and comparison with MODIS collection 4 products. *Remote Sens. Environ.,* **110,** 317–331.

Widlowski, J.-L., and Coauthors, 2007: Third Radiation Transfer Model Intercomparison (RAMI) exercise: Documenting progress in canopy reflectance models. *J. Geophys. Res.,* **112,** D09111, doi:10.1029/2006JD007821.